Cell division Rate Controls Cell Shape Remodeling in Epithelia

John Devany[1], Daniel M. Sussman[2], M. Lisa Manning[2], Margaret L. Gardel[1]

[1]Department of Physics, James Franck Institute and Institute for Biophysical Dynamics, The University of Chicago, Chicago, IL 60637, USA, [2]Department of Physics and Soft Matter Program, Syracuse University, Syracuse, NY 13244, USA

Abstract

Epithelia have distinct cellular architectures, which are established in development, re-established after wounding, and maintained during tissue homeostasis despite cell turnover and mechanical perturbations. In turn, cell shape also controls tissue function as a regulator of cell differentiation, proliferation, and motility. Here we investigate cell shape changes in a model epithelial monolayer. After the onset of confluence, cells continue to divide and change shape over time, eventually leading to a final steady state characterized by arrested motion and more regular cell shapes. Such monolayer remodeling is robust, with qualitatively similar changes in cell shape and dynamics observed in a variety of conditions. However, quantitative differences in monolayer remodeling dynamics reveal underlying order parameters controlling epithelial architecture. For instance, for monolayers formed atop extracellular matrix with varied stiffness, the cell density varies significantly but the relationship between cell shape and motility remain similar. In contrast, pharmacological perturbations can alter the cell shape at which their motility is arrested. Remarkably, across all of these experimental conditions the final cell shape is well correlated to the cell division rate. Furthermore, inhibition of the cell cycle immediately arrests both cell motility and shape change, demonstrating that active stress from cell divisions contributes significantly to monolayer remodeling. Thus, the architecture and mechanics of epithelial tissue can arise from an interplay between cell mechanics and stresses arising from cell division.

Introduction

Cells in epithelial tissues adopt a variety of distinct morphologies which are defined during development and maintained throughout the lifetime of an organism (1). Cellular morphology can be perturbed by stretching or wounding but individual cells within the tissue return to their original shape through increased cellular motility, junctional turnover, neighbor exchange and proliferation (2–5). In turn, tissue architecture impacts cell fate and tissue physiology (6–9). The dynamics of the mechanisms that maintain tissue homeostasis may be important in disease contexts. For example, human bronchial epithelia from asthmatic donors have a much slower rates of structural change than those derived from non-asthmatic patients (7). However, human bronchial epithelial cells divide quite rarely, and so an open question is how cell division and changes to cell density affect cell motility and epithelial tissue structure. Aside from identifying a role for oriented cell divisions (3, 10, 11), we currently lack an understanding of the mechanisms which regulate cell shape remodeling and homeostasis. Such understanding would enable new approaches for tissue engineering and therapeutics.

Epithelial tissue shape and dynamics are determined by the mechanical properties of constituent cells as well as interactions between neighboring cells and with the extracellular matrix. Previous experimental work in actively dividing epithelial monolayers has demonstrated that cell motility is strongly correlated with cell density (12, 13). Particle-based models for tissues (14, 15) successfully explain this result, because an increase in cell density reduces the space available for cells to move past one another, resulting in a collective decrease in cell motion. This leads to a simple, intuitive picture that in proliferating monolayers, tissue homeostasis is directly driven by a change in density that results in cellular crowding and the eventual arrest of remodeling.

However, changes to cell density also regulate signaling pathways that could influence single cell mechanics and cell-cell interactions (16–18). Mitotic divisions themselves also introduce active stress fluctuations (19–22). Thus, the dynamics of cell motion and tissue remodeling could also arise from changes in cell mechanics and active stresses. One promising framework for predicting how cell mechanics and active fluctuations drive collective cell behavior are vertex models, which represent confluent epithelial monolayers by a mechanical network of cell-cell junctions, and have been widely used to understand epithelial mechanics (23–28). These models predict that observed steady-state cell shape, which can be tuned by varying passive cell mechanics and active forces, is an excellent indicator of cell motility (25, 26, 29–32). Indeed, *in vivo* tissue structure is consistent with a local energy minimum of vertex models (27), providing a natural homeostatic mechanism for tissue architecture and shape-dependent dynamic arrest. However, in contrast to particle-based models, confluent vertex models predict that the cell density is not a control parameter for cell dynamics (32). Thus, it remains unclear how cell density, cell mechanics, and active stress fluctuations contribute to the regulation of epithelial monolayer remodeling dynamics.

Here we use epithelial monolayer formation as a model system to investigate the biophysical regulation of epithelial architecture. After forming a confluent monolayer, cells continue to divide and change shape over time, until reaching a final steady state characterized by low motility and more regular cell shapes. Such monolayer remodeling is robust to signaling perturbations, with qualitatively similar changes in cell shape and dynamics over a large range of experimental conditions. To tease apart the effects of cell density changes from other mechanical perturbations, we study monolayers formed atop extracellular matrix with varied stiffness. This variation in substrate stiffness causes the cell densities to change significantly, and we find relatively little correlation of density with cell motion. In contrast, we find a striking data collapse when cell velocities are plotted as a function of observed cell shape, as predicted by active vertex models. To understand whether observed cell shapes are primarily regulated by active fluctuations or by changes to single-cell mechanical properties, we perturb the monolayer with pharmacological interventions that interfere with cell proliferation and the cytoskeleton. We find that

inhibition of the cell cycle immediately arrests cell motion and shape change, suggesting that active stress from cell divisions contributes significantly to monolayer remodeling. Moreover, across all experimental conditions we find that the average cell shape in the homeostatic steady state is well correlated with the cell division rate, suggesting that suppressing cell-division-based fluctuations leads to an arrest of cell motion that is independent of the underlying cell mechanics. Together our results demonstrate that cell geometry and cell division rate control tissue fluidity and cell shape remodeling in epithelial monolayers.

RESULTS

Remodeling of confluent MDCK monolayers to achieve homeostatic architecture

To measure the shape and speed of individual cells in a simple epithelial monolayer we created an MDCK cell line that stably expresses green fluorescent protein localized to the plasma membrane via the transmembrane protein stargazin. We seeded these cells at high density on collagen I gels and imaged multiple fields of view using time-lapse fluorescence microscopy. Initially, the monolayer was not continuous, and there were numerous cell-free voids (Fig.1a.). Over time, the cells closed gaps to form a continuous monolayer spanning ~15 mm; we designate this as t=0 (Fig. 1a). Over the following 12 hours, the cells within the monolayer change shape until a steady-state geometry and density is achieved (Fig. 1a, t=720 min, Movie S1). Thus, we use this as a model system to study epithelial tissue homeostasis by which cell shape and density is recovered after injury through wound healing and monolayer remodeling (Fig. 1b). While previous work has focused on mechanisms of collective migration in wound healing (33–35), here we focus on monolayer 'remodeling' the process by which the average cell shape in a confluent monolayer changes with time.

We use image segmentation to extract cell shape, size, and positions over time (Methods, Movie S1). To quantify cell shape, we use cell vertex locations to reconstruct a polygon with a well-defined perimeter p and area A to calculate the shape parameter (area-normalized perimeter) $q = p/A^{1/2}$; this quantity is bounded from below by objects with a circular shape ($q_{circle} \approx 3.54$), and most cells are observed to have a shape parameter greater than that of a regular hexagon ($q_{hexagon} \approx 3.72$) (Fig. S1) (29, 32). The cell shape, density, and speed all reach a steady-state set of values over the course of approximately 12 hours. Consistent with previous work (13), cell speed decreases (Fig. 1c,d,e , Fig S2) as the density increases from cell proliferation (Fig. 1f). However, we also observe changes in cell shape over time (Fig. 1g), which is correlated with reduced motility in models and experiments where there is no change in density (7, 31). Therefore, from these data alone, the order parameters controlling the steady state cell shape and density in epithelial tissues are impossible to discern.

Cell shape and Speed are correlated in active vertex models

To further understand the process of monolayer remodeling, we explore predictions of a thermal Voronoi model (36, 37). This model is a variation of standard vertex models which incorporates a simple Brownian noise on each cell to account for motile forces applied by the cells. This model has two key parameters (Fig. 2a): a temperature T that represents via uncorrelated noise the magnitude of active force fluctuations acting on each cell, and a parameter p_0 that represents the target perimeter of each cell and encodes the mechanical properties of a cell including tension in the cortically-enriched cytoskeleton and cell-cell adhesions. In steady state, these two parameters give rise to a predicted observed shape parameter and cell mobility (31, 37). We expect that the cells tune their active fluctuations and mechanical properties during monolayer remodeling, resulting in time-dependent parameters $T(t)$ and $p_0(t)$ and different "trajectories" through model parameter space (Fig. 2b).

In general, substantially different trajectories through model parameter space generate fairly similar curves in a plot of typical cell displacements versus observed cell shape, as shown by the solid lines in Fig 2b, c. This is a restatement of the result that, in vertex models, observed cell shape and cell motility are highly correlated (7, 31). In our experiments, we observe a similar relationship between shape and speed resembling these model trajectories (Fig. 2d), suggesting that vertex models may be able to predict features of remodeling in proliferating epithelial layers. Fig 2b, c also highlights that there is an important exception: the observed shape-motility correlation and convergence breaks down when the temperature (i.e. active stress fluctuation) drops to zero while the cell mechanical stiffness encoded by p_0 is still in the floppy regime, with $p_0 \gtrsim 3.8$ (See dashed lines in Fig 2b). In this case, the "zero temperature" system stops moving, even though the underlying mechanics of the layer is floppy and weak. To explore these ideas further, we consider how monolayer remodeling is impacted by perturbation to extracellular or intracellular pathways.

Monolayer remodeling is regulated by matrix stiffness and signaling pathways

The stiffness of the extracellular matrix (ECM), through effects on focal adhesion dynamics and cell spreading, can alter cell migration rates (38, 39). To explore impact on the ECM physical properties on epithelial tissues, we varied the underlying collagen gel stiffness and density by either increasing the concentration of collagen, or crosslinking gels with glutaraldehyde (40, 41). This produced gels with Young's moduli ranging from approximately 200-2000 Pa (42). On all gels, qualitatively similar dynamics in cell shape, motion and density are observed during monolayer remodeling (Fig. S3), but there are quantitative differences. For instance, at the onset of confluence when the cell speeds are large (0.07 μm/min), the cell density is ~50% lower on the stiffer ECM conditions than the soft ones (Fig. 3a, b, Movie S2). These differences remain as the density increases and cell speed decreases during monolayer remodeling (Fig. 3a. b). Thus, across different matrix stiffness, the number density at which cell speed reaches its minimum value varies substantially (Fig. 3b). This is a strong indication that number density is not controlling the arrest of cell motion.

Instead, the cell shapes change robustly and reproducibly during monolayer remodeling, with the arrest of cell motion occurring at a consistent shape parameter of 3.86 (Fig. 3c). These correlations between cell speed and shape are not sensitive to the details of how the time or spatial averaging is performed (Fig. S5). Therefore, cell shape appears to be a robust parameter to predict dynamics and structure of monolayers formed atop different ECM stiffness, in agreement with vertex model simulations. However, vertex models also suggest that shape-velocity curves such as these cannot distinguish between mechanism – active fluctuations, changes to the underlying cell mechanical properties, or some combination of the two generally give the same shape-velocity curves. However, as discussed in the modeling section above, an important exception is if the active fluctuations are driven towards zero while the underlying cell mechanics remains floppy, which can result in a very different curves in shape-velocity space (dashed lines in Fig 2c). To explore this possibility, we next studied the consequences of a wide range of pharmacological perturbations to cell signaling by treatments that altered focal adhesion, cell cycle and Rho GTPase signaling (Movie S3, S4).

Across all conditions, we observe qualitatively similar monolayer remodeling dynamics that result in arrested cell motion with a characteristic cell shape and density (Fig. S3, S5, S6). However, there are substantial quantitative changes that contrast with those found in Fig. 3. To illustrate, we consider the impact of fibroblast secreted growth factors by forming monolayers in fibroblast conditioned medium (FCM). We observed that the cell shapes in FCM-treated monolayers were more elongated, with a higher shape parameter, throughout the experiment (Fig. 4a, Movie S4). At the time of cell arrest, the shape parameter was >3.94 a value which is higher than observed shape in control cells many hours before arrest (Fig. 4b). This resulted in significantly higher values of shape parameters throughout monolayer

remodeling (Fig. 4b). Across the various perturbations to cell signaling and dynamics, we consistently observe a correlation between the changes in shape parameter and cell speed but observe significant variations in the homeostatic shape parameters found in steady state, with perturbed systems arresting at higher values of the shape parameter (Fig. S5, Fig. S6). Comparing to vertex models (Fig 2b,c), this suggests that the arrested cell motion in these pharmacologically perturbed systems occurs because active fluctuations become very small.

Cell division rates control cell shape remodeling

The range of monolayer structures obtained is summarized by determining the steady state, or final, shape parameter and density at the point when cell motion is arrested. The final shape parameter across all experimental conditions is then plotted as a function of the density, and we do not find any clear correlation (Fig. 5a). However, we observed that the cell density increases more slowly for all inhibitors (Fig. S3), indicating a reduced cell division rate. We surmised that changes in cell division rate may be altering the active fluctuations and impacting monolayer remodeling. Across all of the matrix and pharmacological perturbations we tested, the final cell shape parameter shows a strong inverse correlation with the cell division rate (Fig. 5b). Furthermore, monolayer remodeling obtained from another common epithelial model, CACO-2 cells, with a much lower cell division rate, follows this same trend (Fig. 5b, S6).

To explore underlying coupling mechanisms between cell proliferation and monolayer remodeling, we first consider the role of oriented cell divisions. Previous work has demonstrated that oriented cell divisions can also directly change cell shape by producing two daughter cells with lower aspect ratio (3, 10). To access the contribution of oriented division to the overall shape change, we analyzed shape change in individual cells in our segmentation data. We used an algorithm to locate a subset of cell divisions and measured the cell shape of each dividing cell and its immediate neighbors before and after division. Cell division will affect the shape of both the dividing cell and neighboring cells which we classify into three groups based on their contact relationship with the daughter cells (Fig. 5c) We then look at the change in cell shape for each group and a combined average. Similar to previous findings we observe a reduction in the aspect ratio of dividing cells due to division along the interphase long axis (Fig. 5c&d). However, on average, a cell division modestly increases cell shape (Fig. 5e). We further verified through single cell shape trajectories that a large fraction of cell shape change is occurring through junction length changes independent of the division rates (Fig. S7). These data demonstrate that oriented cell division is insufficient to explain the contribution of cell division rate to monolayer remodeling and suggests an alternate mechanism.

Cell Divisions are a source of active stress in the monolayer

Previous work has implicated cell divisions as a source of active stress in epithelial monolayers (14, 19–22, 43). We hypothesize that mechanisms which act independently of active stress generation would occur upstream of mitotic checkpoints. Therefore, we expect that a rapid and direct inhibition of mitosis by inhibiting cyclin dependent kinase 1 (CDK1) activity would reveal direct effects of forces generated by mitosis during monolayer remodeling. Furthermore, CDK1 activity is constrained to the pre-mitotic cell population (44, 45), thereby minimizing potential effects to monolayer mechanics. After initiating a monolayer remodeling experiment, CDK1-containing media was perfused in at t=310 min and then removed at t=580 min. We observed a striking reduction in cell motion within 20 minutes of inhibiting CDK1 (Fig. 6a-c, Movie S5). Upon inhibitor wash out, we observe a sudden increase in cell motion (Fig. 6a+b). We verified that inhibiting cell division by addition of mitomycin C produces similar results (Movie S6). Interestingly, inhibition of cell division by low doses of nocodazole which allows cells to initiate mitotic rounding, but prevents further progress toward mitosis, does not reduce cell speed significantly (Movie S7). This suggests that mitotic rounding or another early mitotic event produces forces sufficient to

5

trigger shape remodeling in neighboring cells, consistent with the increased cortical tension before prometaphase (46).

After removing the CDK1 inhibitor the monolayer remodeling re-initiates, with the changes in shape and speed similar to those initially observed (Fig.6a-c, Movie S5). To quantitatively compare these curves, we shift the post-washout shape parameter data by rescaling the time to (t-400 min); this delay time and rescaling is indicated by dashed lines Fig. 6c&d. Remarkably, with this rescaling the data evolve in almost quantitative agreement with each other and, moreover, are comparable to the evolution of unperturbed wild type monolayers (Fig. 6d). This suggests that inhibiting cell division temporarily reduces activity, but this is reversible upon inhibitor wash out.

DISCUSSION

Here we have characterized remodeling of epithelial monolayers that occurs after the onset of confluence and controls the steady state cell density and shape. The steady state epithelial architecture, including cell shape and density, can be altered by perturbations to extracellular or intracellular cues. Consistent with a thermalized active vertex model, our results show that for monolayers perturbed by differences in substrate stiffness, cell movements attenuate at a certain cell shape, independent of density. Importantly, the experimental data strongly supports the utility of cell shape as an order parameter to assert the arrest of cell movement and local tissue mechanics.

We additionally find that cell divisions are the primary source of active stress driving monolayer remodeling. During division, cells locally increases myosin activity and force generation during mitotic rounding (46) and we suspect this change in cortical mechanics underlies local stress generation. These results highlight an unexpected coupling between cell division and cell shape in monolayers, distinct from oriented cell division. For example, while we demonstrated density does not directly control dynamics, this coupling explains the idea that increasing cell density can arrest epithelial monolayers (12, 13, 47). At high density contact inhibition of proliferation reduces cell division rate (18) which would, in turn, arrest dynamics. While we have demonstrated cell division is necessary for monolayer remodeling, we anticipate that there may also be other interesting molecular mechanisms which couple cell proliferation and cell mechanics during this process (16, 48, 49). Disentangling these effects from the direct effect of forces exerted by dividing cells will be an interesting avenue for future research on cell shape remodeling in epithelia.

We also find that final steady states that result from monolayer remodeling can vary significantly as a result of perturbations to cell proliferation. As the cell division rate is reduced with respect to wild type, the steady state cell shapes become progressively elongated. This connection between cell division and cell motility in the monolayer suggest that active stress is important for monolayer remodeling. Two plausible explanations for this dependence on active stresses are i) that active stress fluctuations approach zero while the preferred cell shapes are still floppy, or ii) additional active stresses beyond those in a standard vertex model are required for cell shape change. Although the first explanation has been highlighted previously in this manuscript as a prediction from a standard vertex model, there is also significant evidence to support the second explanation. The strong correlation of observed shape with the amount of active stress suggest a high sensitivity of junctional remodeling to local stress, not predicted by most current vertex models. One possibility is that this sensitivity to stress arises from energetic barriers to junctional remodeling. In this scenario small but finite fluctuations are not sufficient to cross those dynamical energy barriers, and so the tissue "freezes" into a metastable state even though it is not at zero temperature. Recent work suggests such barriers could arise because cells have signaling-based stress thresholds to junctional remodeling (50). Other aspects of epithelial biology such as mechanical feedback and the long term stability of adherens junctions also suggest that such energy barriers may exist (5, 51). Our data cannot distinguish between these possibilities, and so it would be interesting to study collective

behavior in augmented vertex models that have these additional energy barriers, perhaps in combination with mechanical measurements of interfacial tensions between cells in monolayers.

Our data suggests a mechanism for regulating epithelial mechanics and architecture in different tissues by differential regulation of this turnover rate. Cell proliferation rates can vary widely across different tissues, e.g., the intestine can be entirely replaced after a few days to weeks while the skin may turnover on the timescale of months (52). Moreover, epithelial turnover can be stimulated in response to external chemical and mechanical stimuli, cell death, and tissue damage (53–58). The extent to which cell turnover rate is used to regulate epithelial fluidity and architecture in vivo will be an interesting line of future study. In the chick and xenopus embryos it has been observed that cell division can cause additional neighbor exchanges and as a consequence promotes tissue flows (59, 60). Similarly, recent pipette aspiration experiments in zebrafish development have demonstrated that large changes in tissue viscosity can result from increased rates of proliferation which are required for tissue folding (61). Recent work on cancer and wound healing models have also demonstrated that the EGFR proliferation pathway is required for collective motility (62–64). Measurements of cell shape and motility in these different contexts are required to determine if they are similarly driven by cell division dependent active stress and to discover new mechanisms driving epithelial organization. Further understanding of the interplay between cell division, tissue mechanics and cell shape remodeling may lead to a more comprehensive understanding of tissue function in development, homeostasis and disease.

Materials and Methods: MDCK cells were cultured under standard conditions in DMEM with 10% FBS at 37C and 5% CO_2. Cell monolayers were prepared on by seeding approximately 6×10^5 MDCK cells on a $500mm^2$ collagen gel substrate overnight. Collagen gels were prepared by polymerizing a neutral collagen solution on silane-glutaraldehye modified glass substrates for 1 hour. Cells were imaged by widefield fluorescence microscopy using standard filter sets. We imaged many locations in the monolayer and verified that they show qualitatively similar behavior (Fig S8) Image segmentation, cell tracking and cell division detection were done using custom matlab code based on previous methods (65, 66) and can be made available upon request to the authors. An example of this segmentation can be seen in the supplement (Movie S8). By tracking fixed monolayers we found that the tracking errors are small compared to cell motions (Fig S9). We also found that stage drift is sufficiently small to be corrected for drift by subtracting the mean displacement. Simulations of the thermal Voronoi model were performed as described in previous publications (36, 37). A detailed description of all methods can be found in the supplementary information.

REFERENCES

1. Bissell MJ, Rizki A, Mian IS (2003) Tissue architecture: the ultimate regulator of breast epithelial function. *Curr Opin Cell Biol* 15(6):753–762.

2. Ichijima H, et al. (1993) Actin filament organization during endothelial wound healing in the rabbit cornea: comparison between transcorneal freeze and mechanical scrape injuries. *Invest Ophthalmol Vis Sci*.

3. Wyatt TPJ, et al. (2015) Emergence of homeostatic epithelial packing and stress dissipation through divisions oriented along the long cell axis. *Proc Natl Acad Sci U S A* 112(18):5726–5731.

4. Honda H, Ogita Y, Higuchi S, Kani K (1982) Cell movements in a living mammalian tissue: long-term observation of individual cells in wounded corneal endothelia of cats. *J Morphol* 174(1):25–39.

5. Takeichi M (2014) Dynamic contacts: rearranging adherens junctions to drive epithelial remodelling. *Nat Rev Mol Cell Biol* 15(6):397–410.

6. Miroshnikova YA, et al. (2018) Adhesion forces and cortical tension couple cell proliferation and differentiation to drive epidermal stratification. *Nat Cell Biol* 20(1):69–80.

7. Park J-A, et al. (2015) Unjamming and cell shape in the asthmatic airway epithelium. *Nat Mater* 14(10):1040–1048.

8. Luxenburg C, Zaidel-Bar R (2019) From cell shape to cell fate via the cytoskeleton - Insights from the epidermis. *Exp Cell Res* 378(2):232–237.

9. Watt FM, Jordan PW, O'Neill CH (1988) Cell shape controls terminal differentiation of human epidermal keratinocytes. *Proc Natl Acad Sci U S A* 85(15):5576–5580.

10. Tang Z, et al. (2018) Mechanical Forces Program the Orientation of Cell Division during Airway Tube Morphogenesis. *Dev Cell* 0(0).

11. **Bosveld F, et al. (2016) Epithelial tricellular junctions act as interphase cell shape sensors to orient mitosis.** *Nature* **530(7591):495–498.**

12. **Puliafito A, et al. (2012) Collective and single cell behavior in epithelial contact inhibition.** *Proc Natl Acad Sci U S A* **109(3):739–744.**

13. **Angelini TE, et al. (2011) Glass-like dynamics of collective cell migration.** *Proc Natl Acad Sci U S A* **108(12):4714–4719.**

14. **Ranft J, et al. (2010) Fluidization of tissues by cell division and apoptosis.** *Proc Natl Acad Sci U S A* **107(49):20863–20868.**

15. **Henkes S, Fily Y, Marchetti MC (2011) Active jamming: self-propelled soft particles at high density.** *Phys Rev E Stat Nonlin Soft Matter Phys* **84(4 Pt 1):040301.**

16. **Meng Z, Moroishi T, Guan K-L (2016) Mechanisms of Hippo pathway regulation.** *Genes Dev* **30(1):1–17.**

17. **Irvine KD, Shraiman BI (2017) Mechanical control of growth: ideas, facts and challenges.** *Development* **144(23):4238–4248.**

18. **McClatchey AI, Yap AS (2012) Contact inhibition (of proliferation) redux.** *Curr Opin Cell Biol* **24(5):685–694.**

19. **Doostmohammadi A, et al. (2015) Celebrating Soft Matter's 10th Anniversary: Cell division: a source of active stress in cellular monolayers.** *Soft Matter* **11(37):7328–7336.**

20. **Rossen NS, Tarp JM, Mathiesen J, Jensen MH, Oddershede LB (2014) Long-range ordered vorticity patterns in living tissue induced by cell division.** *Nat Commun* **5:5720.**

21. **Matoz-Fernandez DA, Martens K, Sknepek R, Barrat JL, Henkes S (2017) Cell division and death inhibit glassy behaviour of confluent tissues.** *Soft Matter* **13(17):3205–3212.**

22. **Czajkowski M, Sussman DM, Marchetti MC, Manning ML (2019) Glassy Dynamics in Models of Confluent Tissue with Mitosis and Apoptosis.** *arXiv*.

23. **Alt S, Ganguly P, Salbreux G (2017) Vertex models: from cell mechanics to tissue morphogenesis.** *Philos Trans R Soc Lond, B, Biol Sci* **372(1720).**

24. **Marinari E, et al. (2012) Live-cell delamination counterbalances epithelial growth to limit tissue overcrowding.** *Nature* **484(7395):542–545.**

25. **Staple DB, et al. (2010) Mechanics and remodelling of cell packings in epithelia.** *Eur Phys J E Soft Matter* **33(2):117–127.**

26. **Farhadifar R, Röper J-C, Aigouy B, Eaton S, Jülicher F (2007) The influence of cell mechanics, cell-cell interactions, and proliferation on epithelial packing.** *Curr Biol* **17(24):2095–2104.**

27. **Honda H, Eguchi G (1980) How much does the cell boundary contract in a monolayered cell sheet?** *J Theor Biol* **84(3):575–588.**

28. **Kim S, Hilgenfeldt S (2015) Cell shapes and patterns as quantitative indicators of tissue stress in the plant epidermis.** *Soft Matter* **11(37):7270–7275.**

29. **Bi D, Lopez JH, Schwarz JM, Manning ML (2015) A density-independent rigidity transition in biological tissues.** *Nat Phys* **11(12):1074–1079.**

30. **Lecuit T, Lenne P-F (2007) Cell surface mechanics and the control of cell shape, tissue patterns and morphogenesis.** *Nat Rev Mol Cell Biol* **8(8):633–644.**

31. **Bi D, Yang X, Marchetti MC, Manning ML (2016) Motility-driven glass and jamming transitions in biological tissues.** *Phys Rev X* **6(2).**

32. **Yang X, et al. (2017) Correlating cell shape and cellular stress in motile confluent tissues.** *Proc Natl Acad Sci U S A* **114(48):12663–12668.**

33. **Ng MR, Besser A, Danuser G, Brugge JS (2012) Substrate stiffness regulates cadherin-dependent collective migration through myosin-II contractility.** *J Cell Biol* **199(3):545–563.**

34. **Trepat X, et al. (2009) Physical forces during collective cell migration.** *Nat Phys* **5:426–430.**

35. **De Pascalis C, et al. (2018) Intermediate filaments control collective migration by restricting traction forces and sustaining cell-cell contacts.** *J Cell Biol* **217(9):3031–3044.**

36. **Sussman DM (2017) cellGPU: Massively parallel simulations of dynamic vertex models.** *Comput Phys Commun* **219:400–406.**

37. **Sussman DM, Paoluzzi M, Cristina Marchetti M, Lisa Manning M (2018) Anomalous glassy dynamics in simple models of dense biological tissue.** *EPL* **121(3):36001.**

38. **Doyle AD, Carvajal N, Jin A, Matsumoto K, Yamada KM (2015) Local 3D matrix microenvironment regulates cell migration through spatiotemporal dynamics of contractility-dependent adhesions.** *Nat Commun* **6:8720.**

39. **Bangasser BL, et al. (2017) Shifting the optimal stiffness for cell migration.** *Nat Commun* **8:15313.**

40. **Nimni ME, Cheung D, Strates B, Kodama M, Sheikh K (1987) Chemically modified collagen: a natural biomaterial for tissue replacement.** *J Biomed Mater Res* **21(6):741–771.**

41. **Olde Damink LHH, et al. (1995) Glutaraldehyde as a crosslinking agent for collagen-based biomaterials.** *Journal of Materials Science: Materials in Medicine* **6(8):460–472.**

42. **Lang NR, et al. (2015) Biphasic response of cell invasion to matrix stiffness in three-dimensional biopolymer networks.** *Acta Biomater* **13:61–67.**

43. **Schaumann EN, Staddon MF, Gardel ML, Banerjee S (2018) Force localization modes in dynamic epithelial colonies.** *BioRxiv*.

44. **Heath JR (2001)** *Principles Of Cell Proliferation* **(Wiley-blackwell, Malden, MA). 1st Ed.**

45. **Otto T, Sicinski P (2017) Cell cycle proteins as promising targets in cancer therapy.** *Nat Rev Cancer* **17(2):93–115.**

46. **Ramanathan SP, et al. (2015) Cdk1-dependent mitotic enrichment of cortical myosin II promotes cell rounding against confinement.** *Nat Cell Biol* **17(2):148–159.**

47.   Garcia S, et al. (2015) Physics of active jamming during collective cellular motion in a monolayer. *Proc Natl Acad Sci U S A* 112(50):15314–15319.

48.   Provenzano PP, Keely PJ (2011) Mechanical signaling through the cytoskeleton regulates cell proliferation by coordinated focal adhesion and Rho GTPase signaling. *J Cell Sci* 124(Pt 8):1195–1205.

49.   Clevers H, Nusse R (2012) Wnt/β-catenin signaling and disease. *Cell* 149(6):1192–1205.

50.   Cavanaugh KE, Staddon MF, Munro E, Banerjee S, Gardel ML (2019) RhoA mediates epithelial cell shape changes via mechanosensitive endocytosis. *BioRxiv*.

51.   Charras G, Yap AS (2018) Tensile Forces and Mechanotransduction at Cell-Cell Junctions. *Curr Biol* 28(8):R445–R457.

52.   Hooper CES (1956) Cell turnover in epithelial populations. *J Histochem Cytochem* 4(6):531–540.

53.   Liang J, Balachandra S, Ngo S, O'Brien LE (2017) Feedback regulation of steady-state epithelial turnover and organ size. *Nature* 548(7669):588–591.

54.   Shirakata Y, et al. (2005) Heparin-binding EGF-like growth factor accelerates keratinocyte migration and skin wound healing. *J Cell Sci* 118(Pt 11):2363–2370.

55.   Landén NX, Li D, Ståhle M (2016) Transition from inflammation to proliferation: a critical step during wound healing. *Cell Mol Life Sci* 73(20):3861–3885.

56.   Brock CK, et al. (2019) Stem cell proliferation is induced by apoptotic bodies from dying cells during epithelial tissue maintenance. *Nat Commun* 10(1):1044.

57.   Gudipaty SA, et al. (2017) Mechanical stretch triggers rapid epithelial cell division through Piezo1. *Nature* 543(7643):118–121.

58.   Pinkus H (1951) Examination of the epidermis by the strip method of removing horny layers. I. Observations on thickness of the horny layer, and on mitotic activity after stripping. *J Invest Dermatol* 16(6):383–386.

59.   Firmino J, Rocancourt D, Saadaoui M, Moreau C, Gros J (2016) Cell Division Drives Epithelial Cell Rearrangements during Gastrulation in Chick. *Dev Cell* 36(3):249–261.

60.   Higashi T, Arnold TR, Stephenson RE, Dinshaw KM, Miller AL (2016) Maintenance of the Epithelial Barrier and Remodeling of Cell-Cell Junctions during Cytokinesis. *Curr Biol* 26(14):1829–1842.

61.   Petridou NI, Grigolon S, Salbreux G, Hannezo E, Heisenberg C-P (2019) Fluidization-mediated tissue spreading by mitotic cell rounding and non-canonical Wnt signalling. *Nat Cell Biol* 21(2):169–178.

62.   Lång E, et al. (2018) Coordinated collective migration and asymmetric cell division in confluent human keratinocytes without wounding. *Nat Commun* 9(1):3665.

63.   Palamidessi A, et al. (2019) Unjamming overcomes kinetic and proliferation arrest in terminally differentiated cells and promotes collective motility of carcinoma. *Nat Mater*.

11

64. **Koivisto L, Jiang G, Häkkinen L, Chan B, Larjava H (2006) HaCaT keratinocyte migration is dependent on epidermal growth factor receptor signaling and glycogen synthase kinase-3alpha.** *Exp Cell Res* **312(15):2791–2805.**

65. **Crocker JC, Grier DG (1996) Methods of Digital Video Microscopy for Colloidal Studies.** *J Colloid Interface Sci* **179(1):298–310.**

66. **Asghari MH, Jalali B (2015) Edge detection in digital images using dispersive phase stretch transform.** *Int J Biomed Imaging* **2015:687819.**
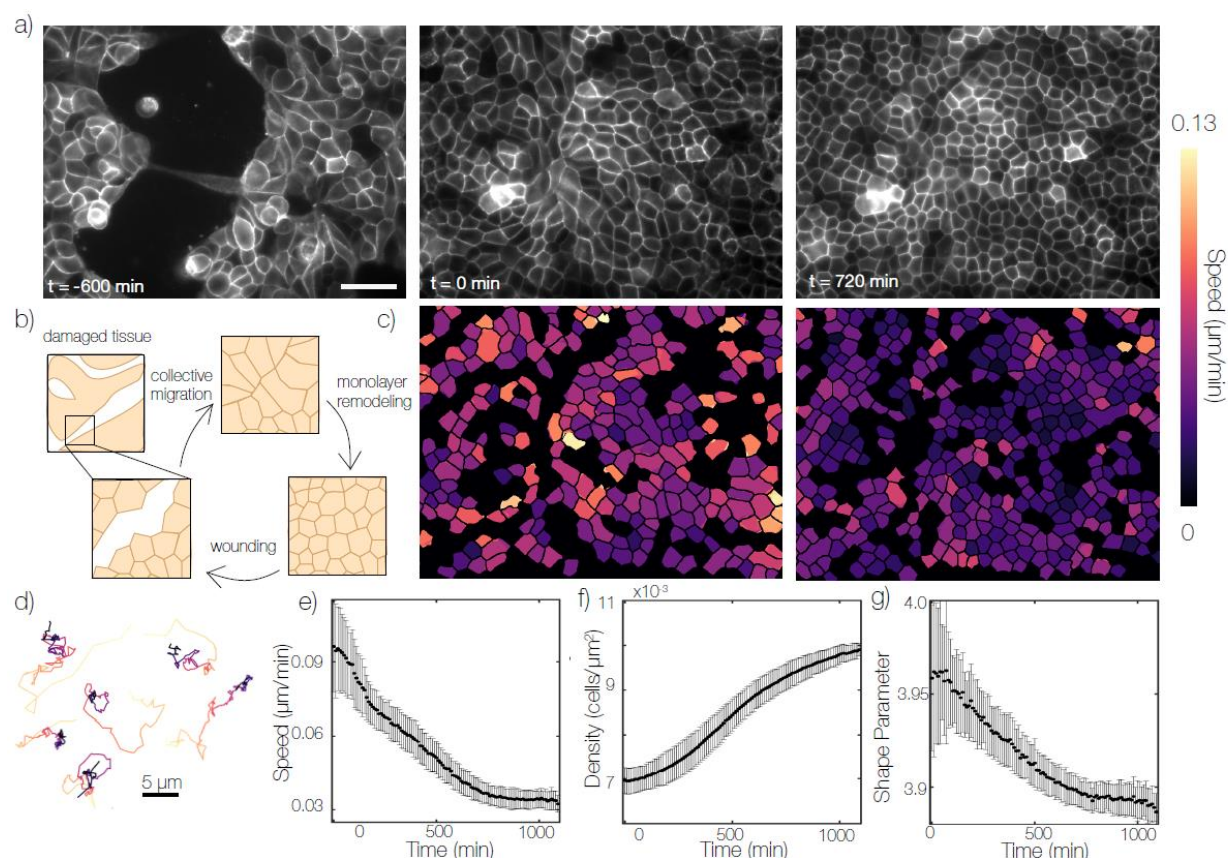
Figure 1: *Cell shape remodeling leads to homeostatic monolayer architecture.* (a) Cells were plated on collagen gel substrates at t= -1000 minutes. By t = -600 minutes cell have aggregated into large colonies which collectively migrate to fill open space. At t=0 minutes cells have formed a confluent monolayer. Over the next 720 minutes cells become denser and cell morphology becomes increasingly regular. Scale bar is 50 microns. (b) Schematic of the process observed in a). A tissue may be wounded resulting in collective migration followed by monolayer remodeling to the normal epithelial architecture. (c) Heat map of single cell speeds plotted over the segmented cell outlines from images shown in a). Areas in black contain cells which were ignored due to potential segmentation errors. (d) Randomly selected cell trajectories from t=0 to t=1100 minutes, color indicates time. (d-f) Sample averaged values of cell shape, speed and density at each time point across 60 fields of view in the sample depicted in a). Error bars represent standard deviation between fields of view.
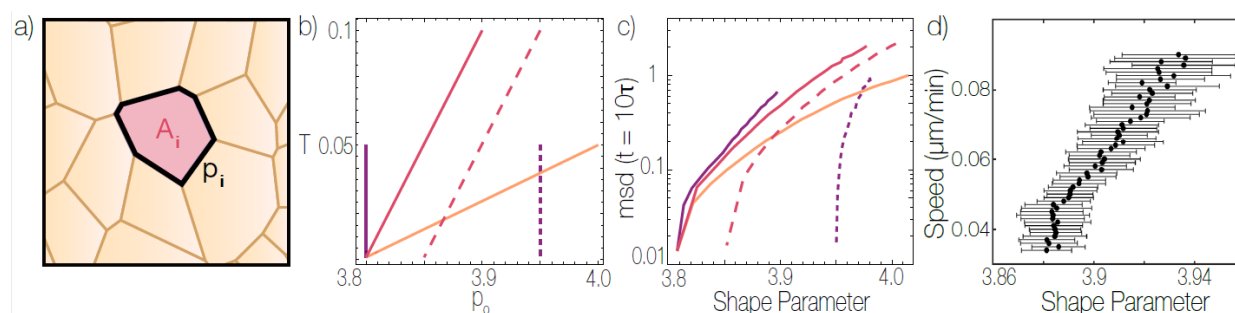
Figure 2: *Active Vertex models predict a relationship between cell shape and speed during monolayer remodeling.* (a) Schematic of the thermal Voronoi model, where each cell has a target geometry specified by a preferred perimeter p_0 and area A_0. Each cell is subject to Brownian noise with amplitude set by the temperature T. (b) Trajectories through parameter space which represent possible trajectories of cell properties evolving during the remodeling of the monolayer. Solid curves approach zero temperature at a value of p_0 where the tissue is rigid, while dashed curves approach T=0 at a value of p_0 where the tissue is floppy (c) Observed values of speed (quantified by MSD in a given time window) and shape corresponding to the parameter space trajectories shown in panel b). MSD is given in units of $\sqrt{\text{Cell Area}}$ over a time window of 10 natural time units (d) Experimental relationship between cell shape and speed measured for WT dataset on 2mg/ml collagen matrix.
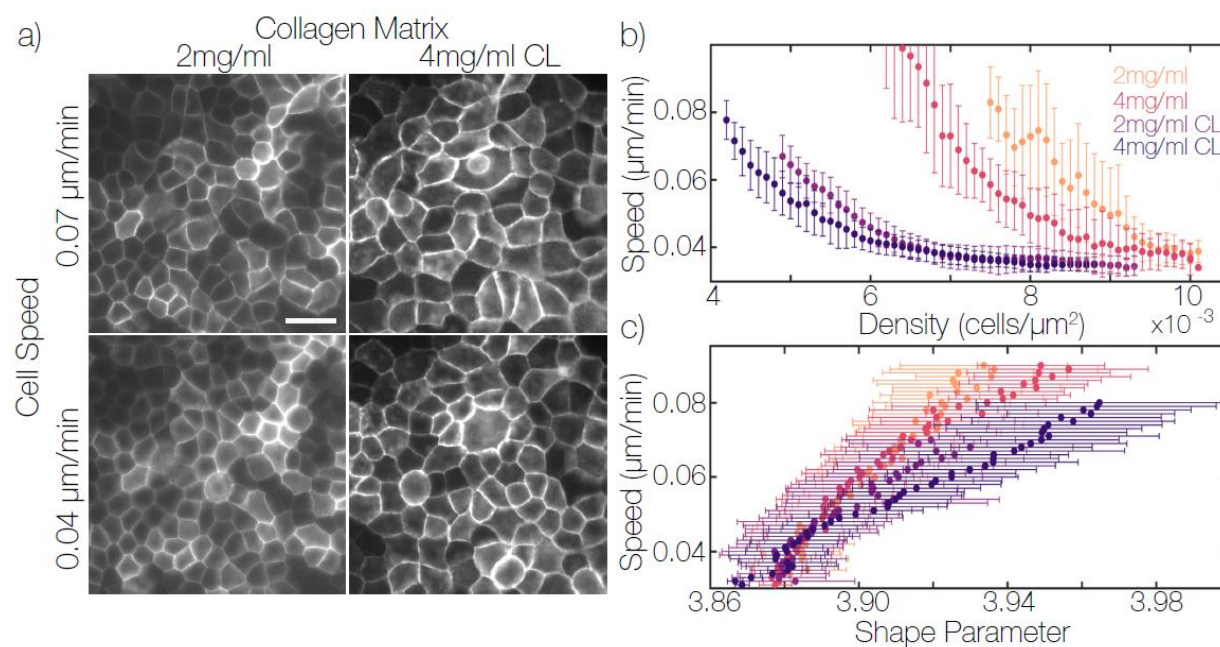
Figure 3: *Monolayer remodeling is independent of cell density across perturbations to substrate stiffness.* (a) Images of monolayers remodeling on substrates with different stiffness near the beginning and end of the experiment. CL is glutaraldehyde crosslinked collagen gel. (b) Correlation between cell speed and cell density for monolayers on substrates of different stiffness. (c) Correlation between cell speed and shape parameter for monolayers on different substrates. Quantities are averaged over a field of view containing at least several hundred cells for each time point, then field of view measurements are binned together by speed in 0.001 increments. Error bars represent standard deviation of each bin.
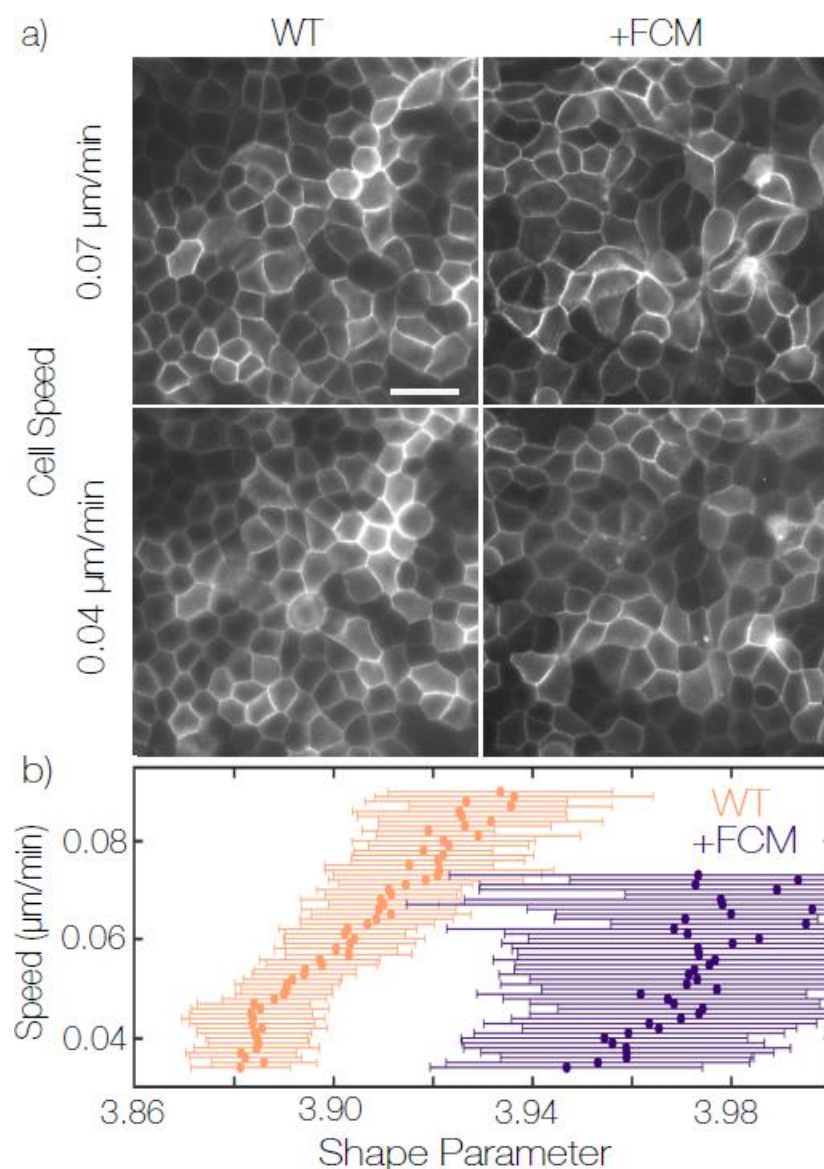
Figure 4: *Intracellular signaling alters cell shape during monolayer remodeling* (a) Images of monolayers at the beginning and end of a remodeling experiment under WT conditions or treated with 1:1 fibroblast conditioned medium to culture medium. (b) Correlation between speed and density for control and FCM treated monolayers. Quantities are averaged over a field of view containing at least several hundred cells for each time point, then field of view measurements are binned together by speed in 0.001 increments. Error bars represent standard deviation of each bin.
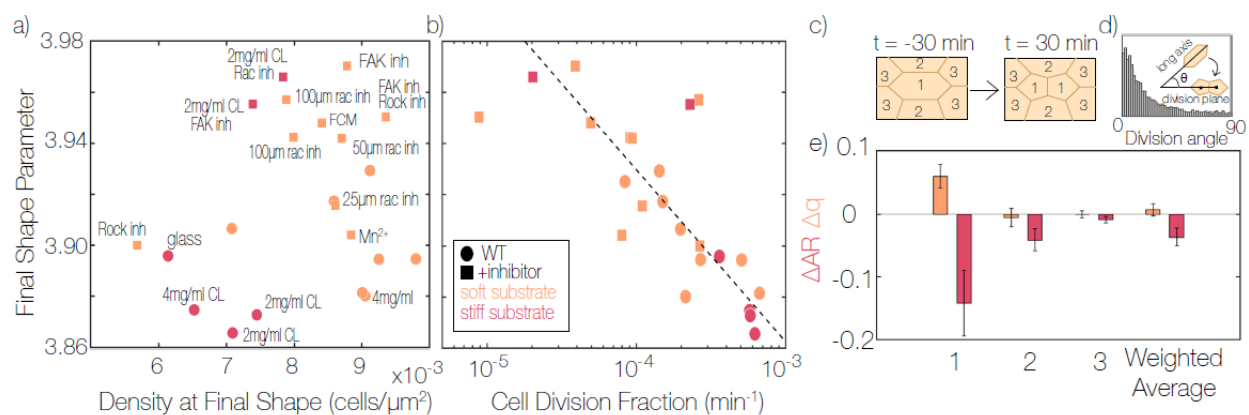
Figure 5: *Cell shape remodeling is dependent on cell division rate* (a) Shape parameter vs. density when the monolayer reaches a speed of 0.04µm/min for all inhibitor conditions tested. (b) Final shape parameter vs. the cell division rate from t=200 min to t=600 min for all conditions in a). Logarithmic fit to data is plotted at dashed line. Each data point in a) and b) are the average of >10 time points after reaching the final shape from >30 fields of view from one experiment. (c) Schematic of cell which may experience direct changes in geometry during cell division. 1 is the dividing cell, 2 is a neighbor of both daughter cells, 3 is a neighbor of one daughter cell (d) Histogram of measured angle between the cells interphase long axis and the division plane during WT experiments. (n=3137 cell divisions) (e) Resulting changes in shape and aspect ratio for the dividing cells and neighbors adjacent to one or both cells are plotted. Error bars represent the standard deviation of three WT experiments on 2mg/ml collagen each with at least 1000 cell divisions measured.
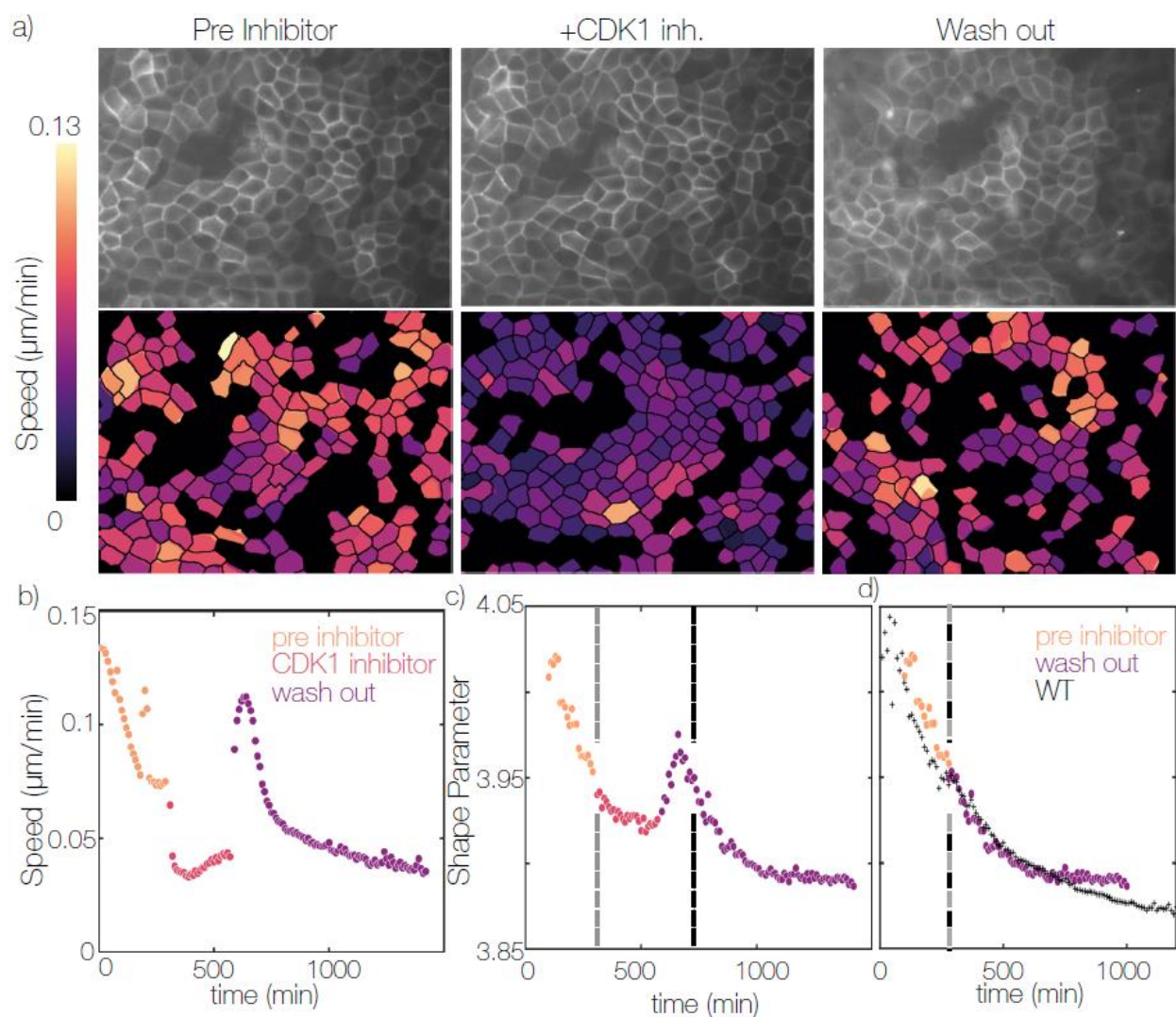
Figure 6: *Cell division is a source of active stress required for monolayer remodeling.* (a) Representative field of view of monolayer during CDK1 inhibitor wash in experiment. Below each image heat maps of cell speed for successfully segmented cells are displayed. (b) Average cell speed vs time during CDK1 inhibitor wash in experiment. (c) Average cell shape vs time during CDK1 inhibitor wash in experiments. (d) Time shifted shape vs time curves comparing WT and CDK1 inhibitor wash in data. CDK1 inhibitor wash in data points represent the time average of 12 fields of view in one sample. WT data represents the average of 3 independent experiments each with >20 fields of view. CDK1 inhibitor is 5µM RO-3306.

Supplementary Information for:

Cell division Rate Controls Cell Shape Remodeling in Epithelia

John Devany[1], Daniel M. Sussman[4], M. Lisa Manning[4], Margaret L. Gardel[1,2,3]

Department of Physics[1], James Franck Institute[2] and Institute for Biophysical Dynamics[3], The University of Chicago, Chicago, IL 60637, USA, Department of Physics and Soft Matter Program[4], Syracuse University, Syracuse, NY 13244, USA

This PDF contains
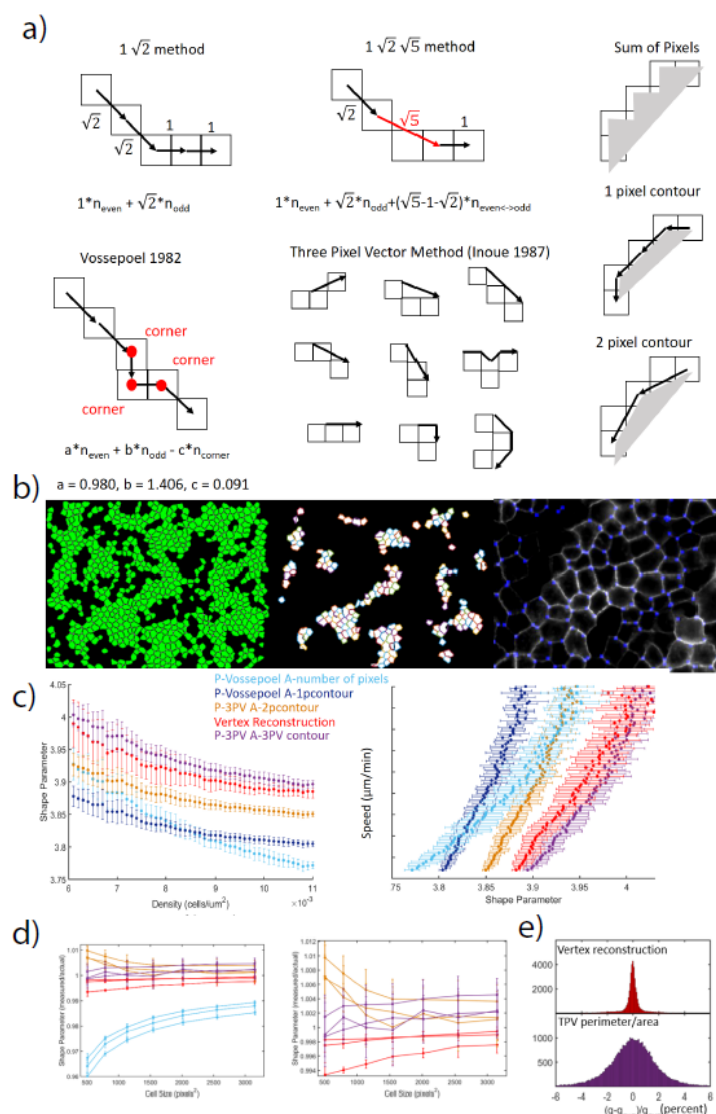
Supplemental Figure 1: *Shape metrics are resolution dependent.* (a) Schematics describing different popular methods for determination of perimeter and area of a polygon constructed from pixels. Methods depicted include the 1 root 2 method – default in imageJ, and voesspoel – default in Matlab regionprops. We also schematize several methods for determining polygon area. Sum of pixels is default in both imageJ and Matlab (b) An image of cell outlines (green) with marked vertex locations (pink). The cells which do not have a complete set of neighbors are discarded and remaining polygons are constructed from the vertices. We show an overlay of detected vertices on the raw data. (c) For one experimental dataset, WT on 2mg/ml collagen – we plot shape vs density for a variety of shape metrics and Speed vs shape for the same set of metrics. Errorbar represents the standard deviation of 60 fields of view. (d) We segmented simulation data and plot shape/actual shape vs area for this data for a variety of shape metrics for images of different resolution. We observe that some shape metrics show large errors and are highly resolution dependent. We show a zoom in of the top performing metrics. Error bar represents the standard deviation of three replicates (e) We measured shape of fixed cell data and used the two top performing metrics to measure cell shape. The fixed data is a time series of images where there is no cell motion but images show photobleaching and noise variation. We know the shapes are not changing with time, however the measured shape fluctuates due to changes in noise. We measure the distribution of

2

measurements around the mean for the two metrics for each cell. Shapes reconstructed from vertices are much more robust to noise.
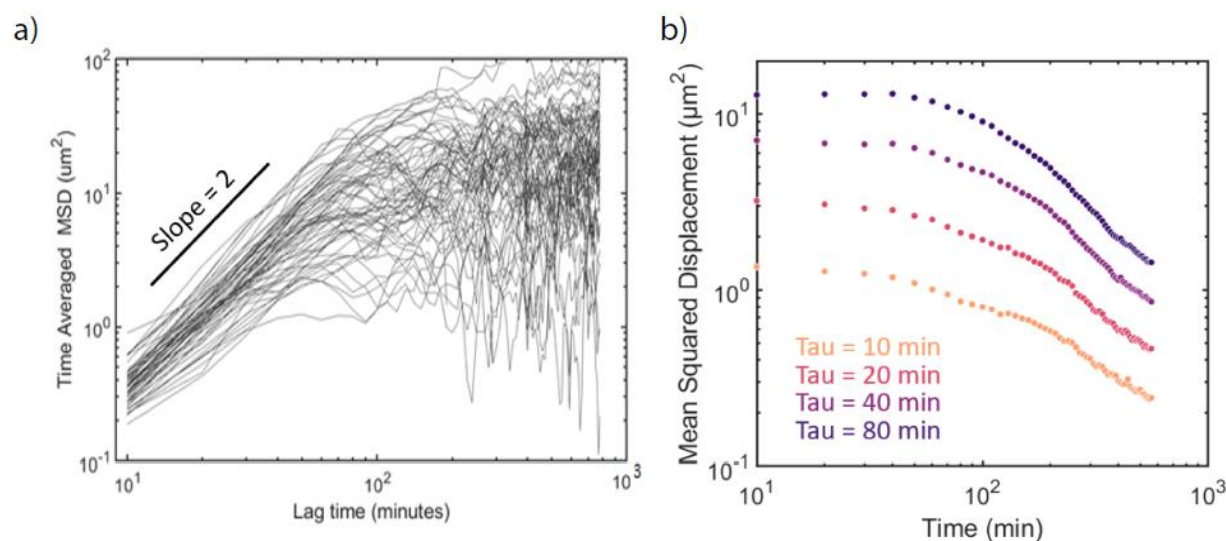
Supplemental Figure 2: *Mean square displacements are time dependent.* (a) Time averaged mean squared displacements for individual cells show a plateau at long time scales indicating cells are not freely moving at long times. A small representative subset of 100 cells from one field of view is displayed (b) mean squared displacement for different lag times decay with time indicating that cell motion is reduced at later times. Data is across all cells in 60 fields of view in a single single experiment on a 2mg/ml collagen gel under wild type conditions.
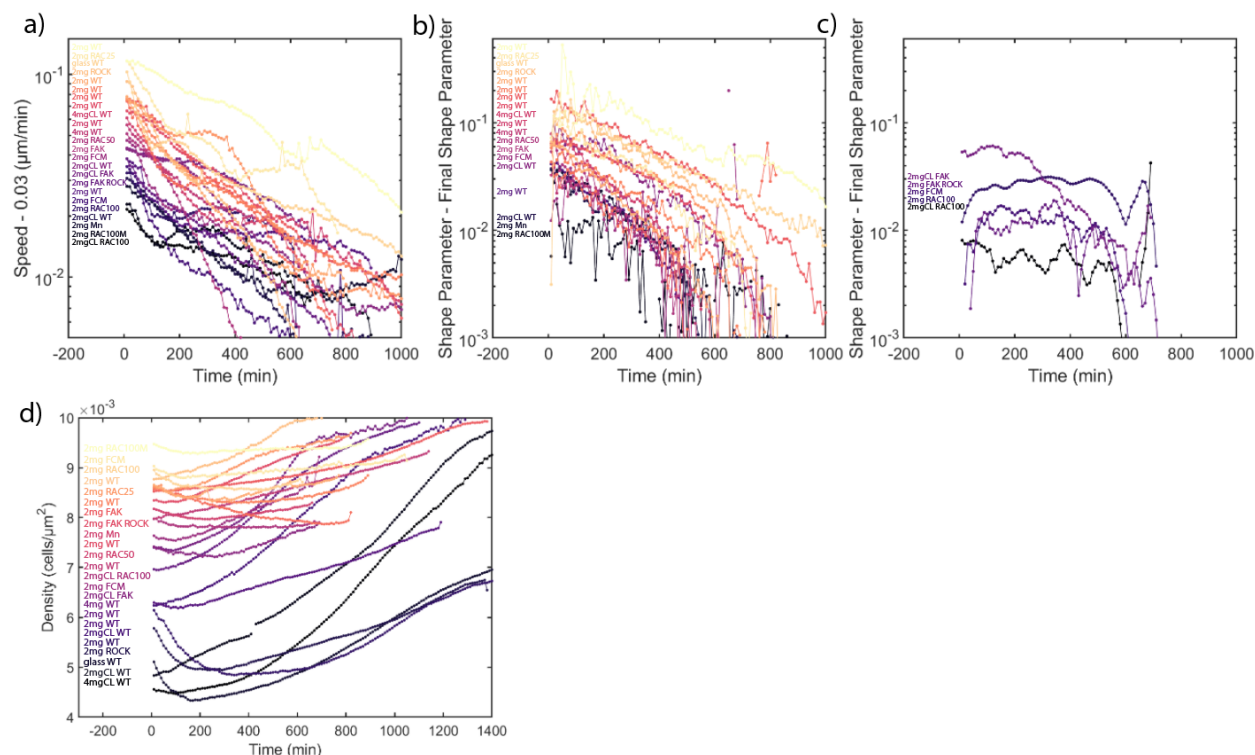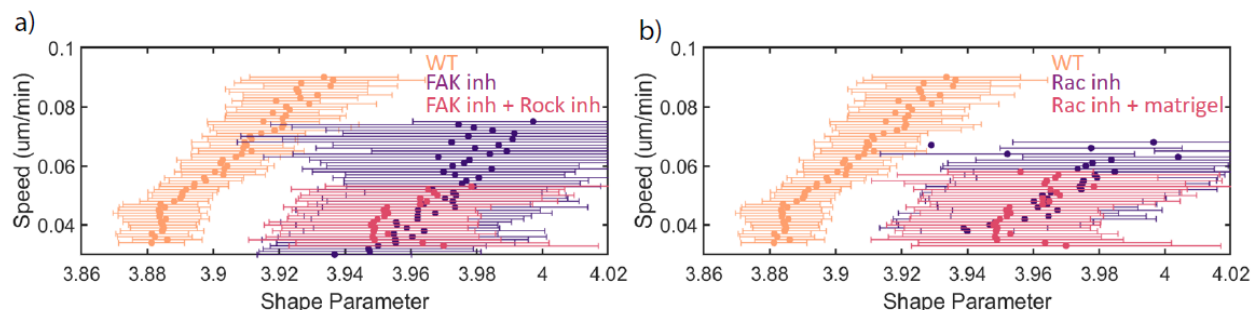
Supplemental Figure 3: *Shape, Speed and cell area decrease with time across all conditions* (a) plot of speed vs time for all conditions in figure 2b. The final speed for all the time series plateau at 0.03um/min so this value is subtracted from each time series. Curves are colored in order of speed at time = 0 min. The same color map is used in b ,c (b) plot of shape-final shape for all data. Each time series decays to the final shape with similar kinetics. (c) several datasets were too noisy and were moved to a different plot for clarity. These datasets were smoothed temporally with a 10-point window to reduce noise. These data slightly reduce in shape with time however the difference in initial and final shape are comparable to the noise in our measurement. (d) density vs time for all datasets. The data is colored by initial density and differs in color map from a-c. All data points represent the time average of at least 30 fields of view in one sample.
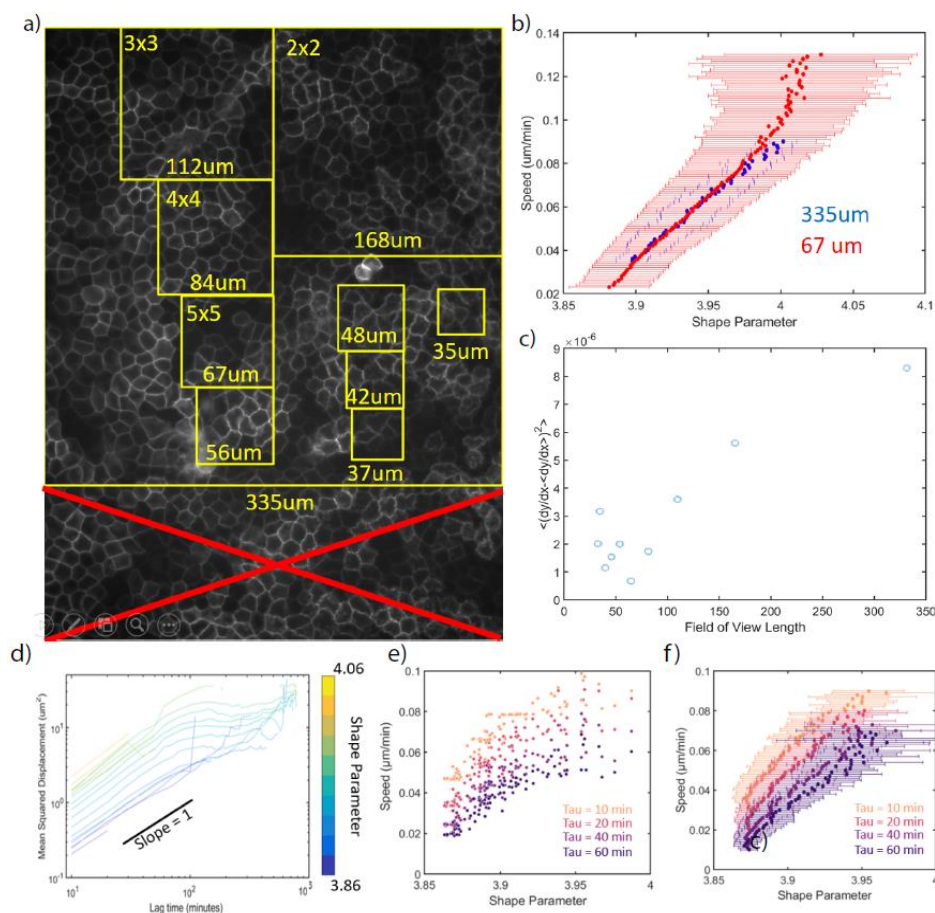
Supplemental Figure 4: *Correlation between shape and speed does not depend on the field of view size or time between images.* (a) representation of different field of view sizes. For this analysis the field of view was first truncated into a square window 335x335 µm. This field was subdivided into 2x2, 3x3… 10x10 sections and each section was averaged independently as if that was the full field of view. (b) speed vs shape parameter for the full field of view 335x335 µm and a 5x5 truncation 67x67µm. Both field of view sizes show the same final average. All other truncation sizes give the same average values. Errorbars represent the standard deviation of 60 and 1500 fields respectively (c) comparison of the derivative in the linear portion of the curve in b, from q=3.93 to q = 3.97. The value is larger for large fields of view because there can be greater heterogeneity within the same field of view. At lower values the linearity plateaus due to noise from averaging fewer cells. This shows that our data is consistent with energy which is defined at the single cell level. At ~100um or groups of a couple dozen cells we reach a noise floor. This analysis uses the TPV metric for cell shape to ensure there are enough cells within small fields of view to get a representative average. (d) Mean squared displacement for a dataset on a WT 2mg/ml collagen gel. Curves are binned according to the shape parameter at the initial time of each subtrajectory. Subtrajectories are not overlapping. Lag times are at 10 minute intervals. We observe that for any lag time there is lower displacement for lower shape parameter. (e) Shape parameter vs speed for a single field of view over 12 hours for different lag times. (f) Shape parameter vs speed averaged across all fields of view in the sample. We see that increasing the lag time shifts this curve downward consistent with the motion being diffusive. At longer times the distance traveled only increases by sqrt(t) as time increases by t leading to lower values of speed. The data appears to reach the noise floor at low shape parameter for larger tau.

6
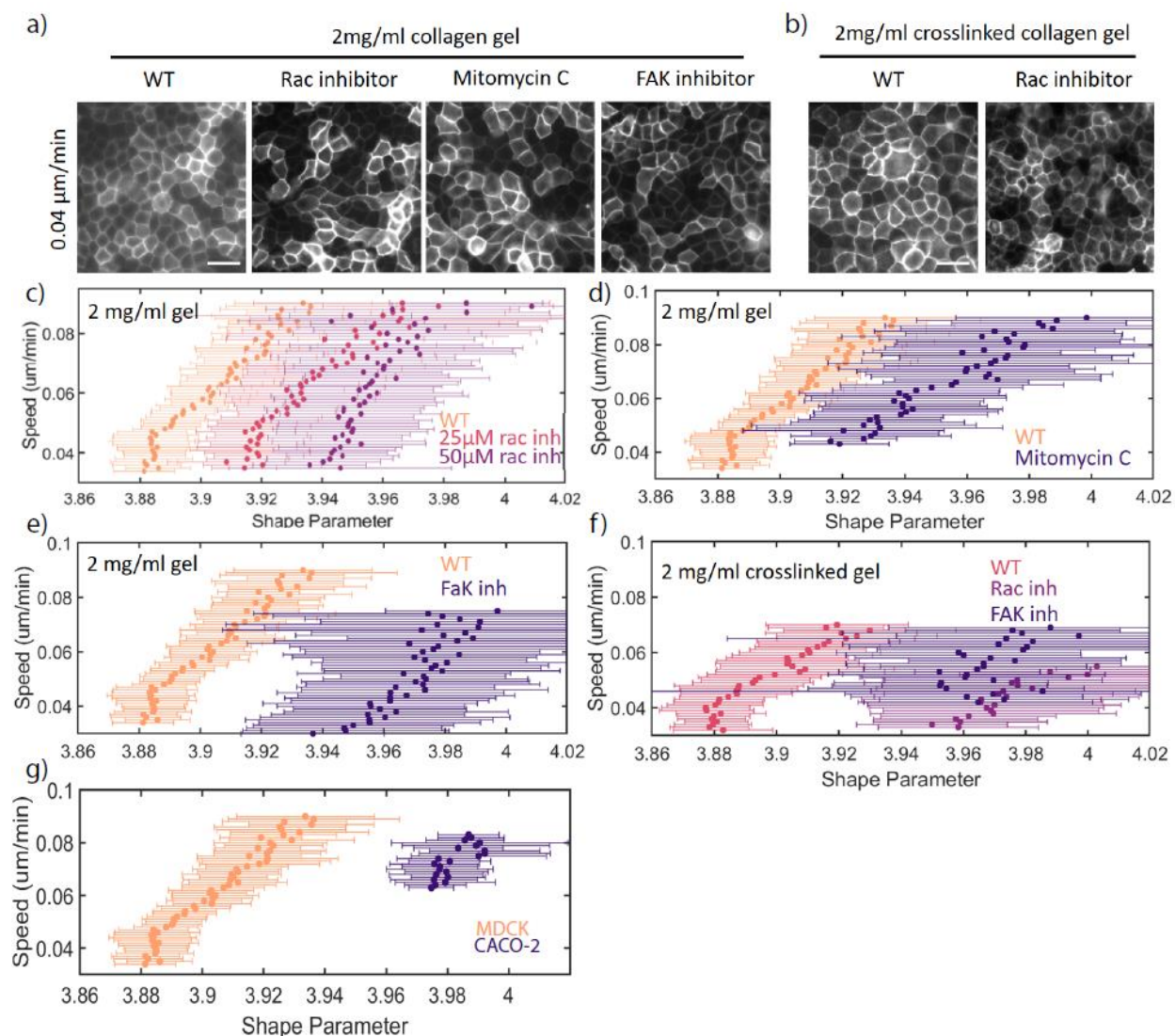
Supplemental Figure 5: *Shift in relationship between shape parameter and speed is qualitatively similar across conditions.* (a) Representative images for several inhibitor conditions at low average speed. (b) Images on stiff substrates (c-e) Speed vs Shape parameter curves for different inhibitors. Similar shifting behavior is observed across these conditions. (f-g) Similar behavior is also observed on stiff substrates and for CACO-2 epithelial cells. Errorbars represent binned averages at each speed for at least 30 fields of view over at least 60 time points.

7

Supplemental Figure 6: *Rescue experiments do not restore shape speed correlation.* (a) Comparison of shape speed correlation for cells treated with a FAK inhibitor and with the addition of a Rock inhibitor. Rock inhibition has been observed to rescue the polarity of 3D MDCK cultures with FAK knockdown. Rock inhibition has also been observed to restore collective motility in FAK knockdown cells (see discussion). (b) Comparison of shape speed correlation for cells treated with a RAC inhibitor on collagen gels and collagen gels with 1mg/ml matrigel. RAC is required for the assembly of laminin at the basal surface of 3D cultures of MDCK cells. The polarity defect of RAC knockdown cells can be rescued by providing laminin, a component of matrigel, in the substrate (see discussion). Neither experiment significantly restored the correlation between shape and speed. Errorbars represent binned averages at each speed for at least 30 fields of view over at least 60 time points.
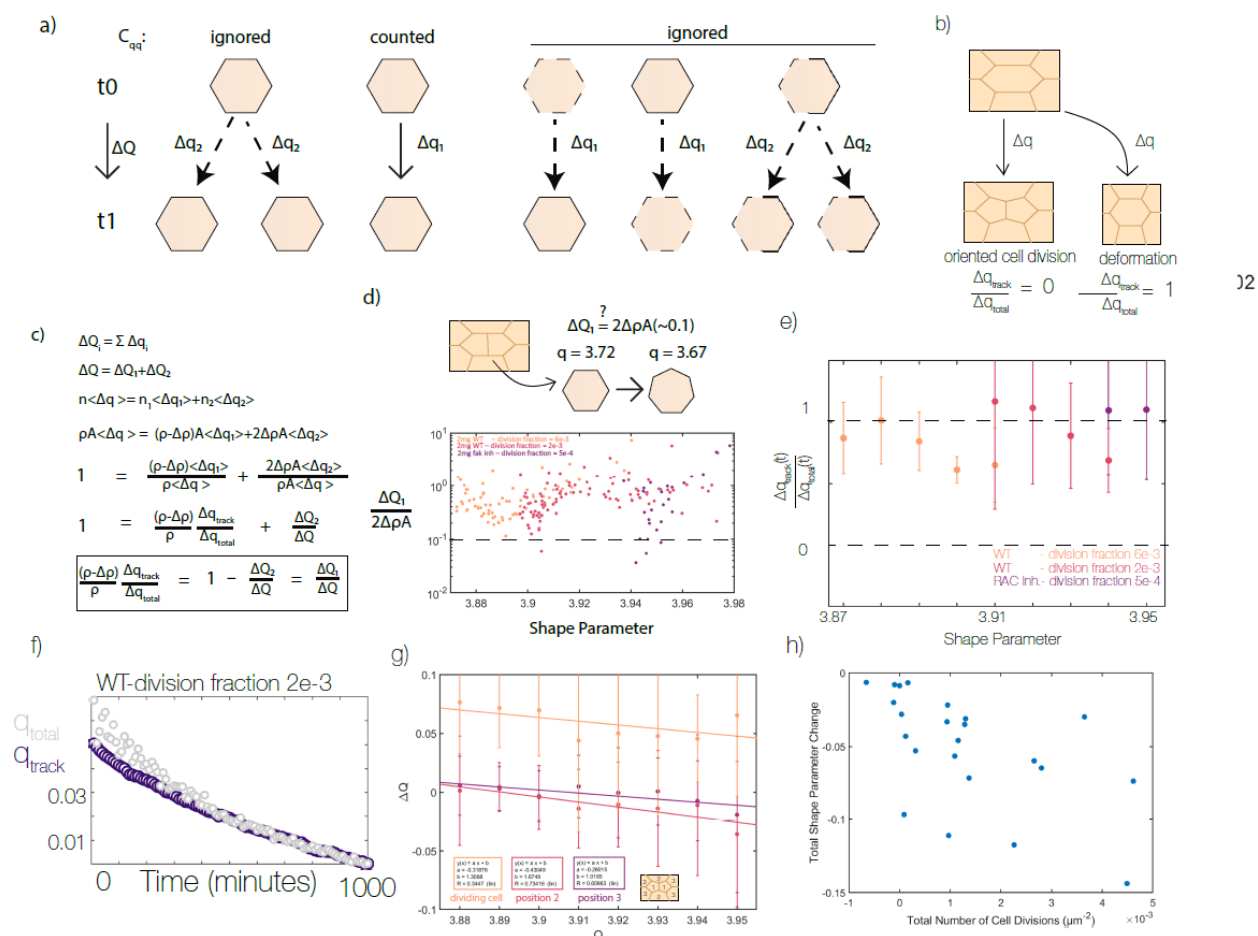
**Supplemental Figure 7:** *Oriented division is insufficient to explain differences in monolayer remodeling* (a) Schematic of different modes of shape change – either shape changes during a cell division Q2 or within a trajectory Q1. There are additional q1 type and q2 type shape changes which are ignored by cqq. (b) schematic of different sources of cell shape change and their relative values of q_{track} (c) Under the assumption that cells which are segmented in consecutive frames have average shape change representative of all cells, we show that the q_{track}, average shape change and density which are all measured in the experiment can report on the average shape change through oriented division (d) Our metric has ignored the gain of neighbors for cells adjacent to division. We show that the value of q_{track} is several fold larger than this effect. Points represent time averaged values for at least 50 fields of view (e) ratio of q_{track} to q_{total} for three different conditions with variable division fraction noted in the legend. We observe in all cases that the ratio is close to 1 independent of cell shape. Errorbars represent standard error of each bin. (f) for a single condition we plot q_{track} and q_{total} over time. We observe that for most of the experiment these metrics are the same. (g) average shape change per cell division from division tracking data as a function of the average cell shape. We observe larger decreases in cell shape when for the mother cell and neighbors when average cell shape parameter is large. Errorbars represent standard deviation of divisions in each bin (h) plot of total cell division vs total shape change. If cell divisions cause all shape change, we would expect a strong correlation between these variables. Each point represents a different condition from Fig 5a.

9
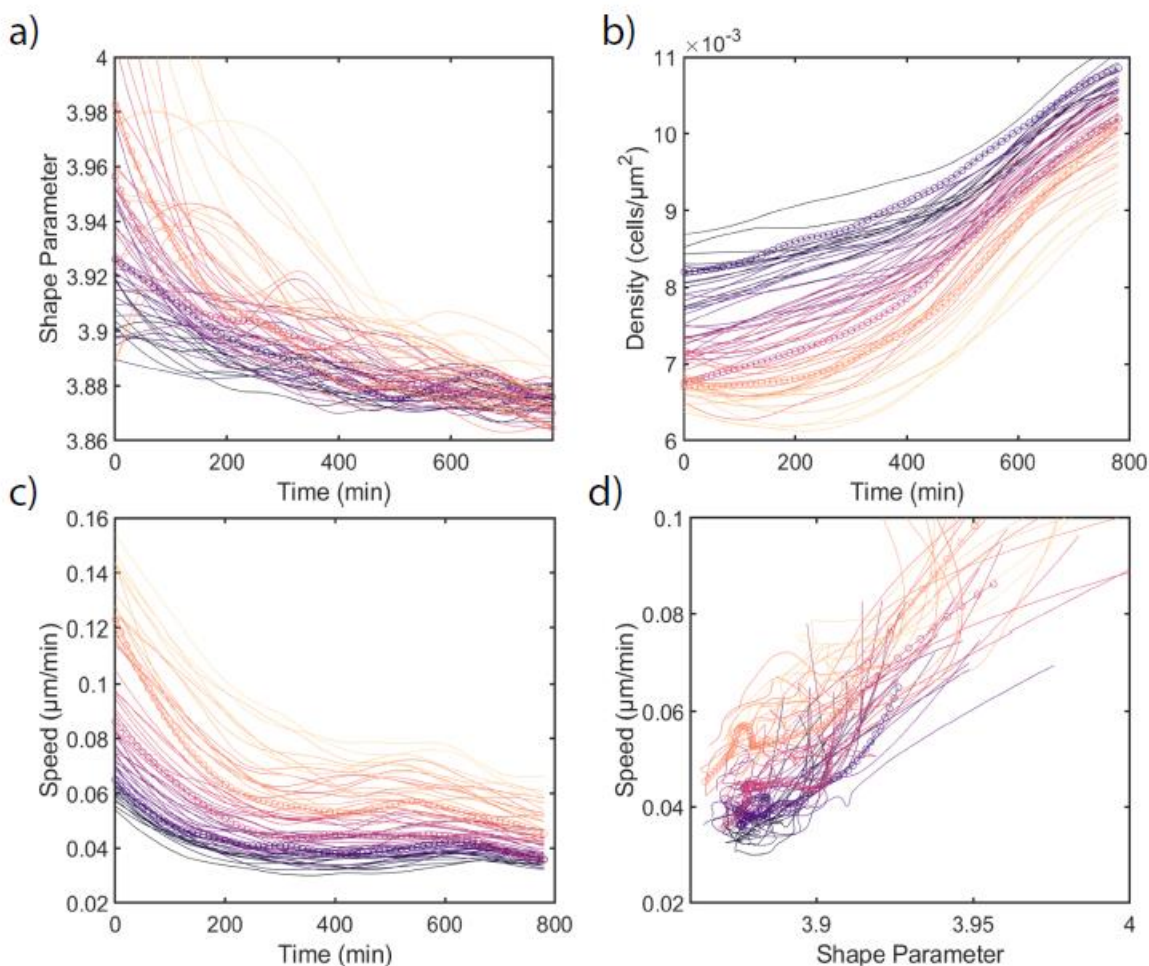
Supplemental Figure 8: *Different fields of view across the sample are qualitatively similar to the mean.* (a) values of shape parameter for each field of view over time (b) density against time for the same set of fields of view. (c) speed vs time for the same set of fields of view (d) shape vs speed for the same set of fields of view. Time points are taken every 10 minutes. Data is colored according to the initial speed in the field of view. Colors are consistent across all panels. We see that the datasets which have larger initial speed also have larger initial shape and lower initial density.
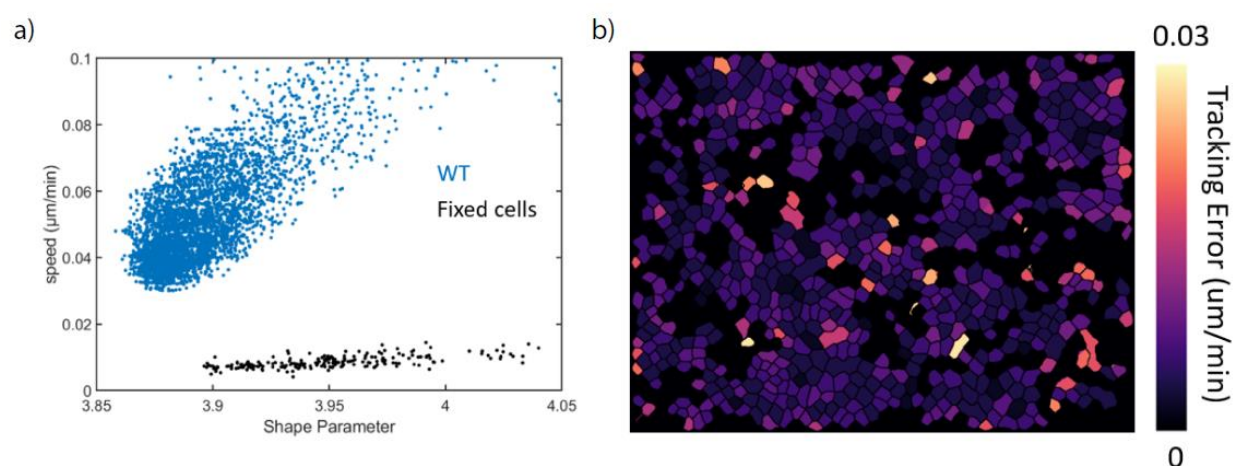
Supplemental Figure 9: *Characterization of lower bound for noise floor* (a) relationship between shape and speed in WT data on a 2mg/ml collagen gel and under the same conditions but fixed in 4% PFA for 10 minutes before imaging. We observe an estimated noise floor with minor shape dependence and average value well below the speeds measured in the experiment. The noise floor may be larger due to larger fluctuations in protein levels and cell heights in live samples. Points represent the average cell shape and speed at a single field of view and time point (b) heat map of perceived displacements in fixed data. Measurement error is fairly homogeneous and very few single cells tracking errors comparable to experimental displacements.
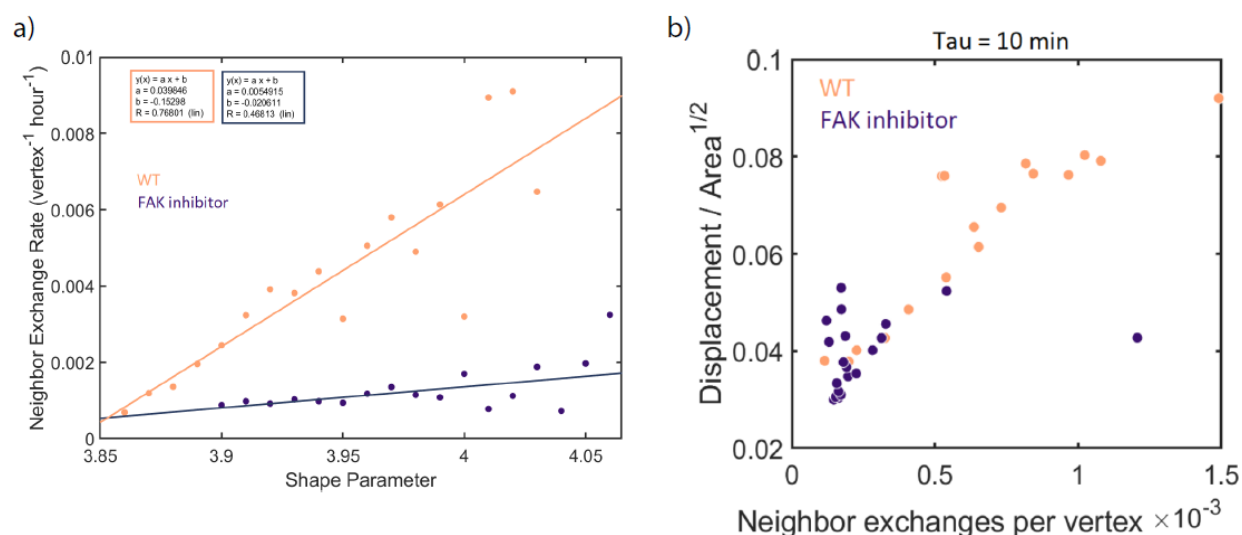
Supplemental Figure 10: *Neighbor exchange rates depend on shape and cell division rates* (a) Neighbor exchange rate vs shape for WT and FAK inhibited cells on 2mg/ml collagen gels. Neighbor exchanges were counted by identifying 4 fold vertices in the data. A 4-fold vertex represents an unstable configuration in the system and therefore will either resolve in the opposite direction it was formed (successful exchange) or back in the same direction (failed neighbor exchange). Our method does not differentiate the two types of neighbor exchange. Each point is the ratio of four fold to three fold vertices detected at the given average shape parameter across at least 50 fields of view and 80 time points in each condition. (b) relationship between neighbor exchange rates and measured cell speed for data points in a)

12

SI methods:

Reagents: PND1184, Nocodazole, y27632, NSC23766, Mitomycin C, Human Transferrin, (3-Aminopropyl)trimethoxysilane were purchased from Sigma-Aldrich (Saint Louis, MO), Glutaraldehyde purchased from Electron Microscopy Sciences (Hatfield, PA), BD Collagen I, rat tail was purchased from BD Biosciences (San Jose, CA). 1X PBS, 1X DMEM, Fetal Bovine Serum, l-glutamine, Penicillin-Streptomycin, Trypsin EDTA were purchased from Corning Inc. (Tewksbury, MA), TBS, MnCl, NaOH were purchased from Fisher Scientific (Hampton, NH), Ro-3306 was purchased from Cayman Chemical (Ann Arbor,MI)

Cell culture: Madin-Darby Canine Kidney (MDCK) cells and Mouse Embryonic Fibroblasts (MEFs) were cultured in high-glucose DMEM supplemented with 10% FBS, 2mM L-glutamine, 100 U/mL penicillin, and 100 μg/mL streptomycin at 37C and 5% CO_2. Caco-2 cells were cultured in DMEM supplemented with 10% FBS, 2mM L-glutamine, 100 U/mL penicillin, and 100 μg/mL streptomycin and Human Transferin at 37C and 5% CO_2. Cells were passaged using 0.25% trypsin EDTA every 2-3 days. Cells were checked for mycoplasma by Hoechst staining.

Stargazin-GFP MDCK cells we produced by transient transfection of WT MDCK cells with a PiggyBac-stargazin-GFP construct followed by selection by puromycin and subcloning. A clone with high expression of the marker and similar morphology to WT MDCK cells was selected for experiments. Stargazin-halotag Caco-2 cells were produced by lentiviral infection of WT CACO-2 cells by a WPT-Stargazin-halotag construct packaged in 293T cells by a second generation lentiviral system with rev8.2 and VSVG. Cells were sorted by a flow cytometer into single cell wells and a clone with high expression and normal CACO-2 morphology was selected for experiments.

AminoSilane Glutaraldehyde modification of glass coverslips: Glass coverslips were modified as previously described to couple collagen gels to the surface of the glass (Zhu et al., 2012). Coverslips were first cleaned by sonication in 70% and 100% ethanol solutions then dried with compressed air. We placed coverslips in a staining rack and submerged the rack in a solution of 2% (3-Aminopropyl)trimethoxysilane (APTMS) 93% propanol and 5% DI water for 10 minutes at room temperature while stirring. Staining racks were removed and washed in DI water 5 times then placed in a 37C incubator for 6 hours to allow the water to dry and aminosilane layer to cure. The staining racks were then submerged in 1% glutaraldehyde in DI water for 30 minutes while stirring. Then the samples were washed 3 times for 10 minutes in distilled water, air dried and stored at room temperature. Activated coverslips were used within 2 months of preparation.

Collagen gel preparation: 10x PBS, milli-q filtered water, a 5mg/ml collagen stock and 1N NaOH were mixed to generate a polymerization mix with 1xPBS and 2 or 4 mg/ml collagen at neutral pH. To visualize collagen gel thickness we produced a fluorescently labeled collagen stock by mixing collagen with alexa647-NHS ester in 0.02M acetic acid overnight. We added fluorescently labeled collagen at a 20:1 ratio to unlabeled collagen in the polymerization mix. 70uL of the polymerization mix was added on to a 25mm round modified coverslip and quickly spread to coat the surface using a pipette tip. Samples were transferred to a humidified incubator at 37C to polymerize for 1 hour. After polymerization gels were washed 3 times in 1x PBS and it was verified that gels were still intact and adhered to the glass by a tissue culture microscope.

Glutaraldehyde crosslinked gels were prepared as above and crosslinked as previously described (Lang et al., 2015). Directly after polymerization and washing gels were incubated in 1xPBS containing 0.2% glutaraldehyde for 30 minutes. Gels were then washed quickly 3 times in 1xTBS, washed in 1x TBS at 1 hour intervals 5 times and left in 1x TBS overnight to quench excess crosslinking groups on the gel. The gels were then washed in 1x PBS three times. All gels were used within 2 days of polymerization.

Monolayer preparation: Monolayers were formed on collagen I gel to study monolayers under more physiologically relevant conditions than typical glass, plastic or hydrogel surfaces (Bissell, 1981; Elsdale and Bard, 1972; Simons and Fuller, 1985; Walpita and Hay, 2002; Yu et al., 2016). Cells were seeded onto collagen gels at high density (~600,000 cells on 500mm^2 surface) such that cells coated ~70% of the gel surface at seeding. The sample was returned to the incubator overnight (8-12 hours) before the experiment. For inhibitor treated conditions the inhibitor was added 10-20 minutes after the cells were seeded on the gel to allow cells to attach before adding fluid volume. Before mounting samples, the monolayer was viewed under a tissue culture microscope and continuously covered a region 10-15 mm across. Samples were washed 3 times with 1x PBS and quickly mounted into a sealed round chamber with 1.5mL of culture media and with equal concentration of inhibitor to at seeding. Before taking each time lapse the collagen gel was verified by fluorescence microscopy to be homogeneous and 150-250 µm thick. The monolayer was confirmed to extend at least several hundred microns in each direction outside selected fields of view. By only observing cells more than a few hundred microns from a free edge we avoid the increased migration speed and correlation from cytoskeletal assemblies specific to wound healing (Ng et al., 2012; Trepat et al., 2009).

Fluorescence microscopy: Cells were imaged on an inverted epi-fluorescence microscope (Nikon TI-E, Nikon, Tokyo, Japan) with a 20x plan flour multi-immersion objective. Glycerol was used as an immersion medium to more closely match the index of refraction of the collagen gel. Images were acquired at 10 minute intervals in GFP, 642 and transmitted light channels using standard filter sets (Ex 490/30, Em 525/30, Ex 640/30, DAPI/FITC/TRITC/cy5 cube) (Chroma Technology, Bellows Falls, VT). Samples were mounted on the microscope in a humidified stage top incubator maintained at 37C 5% CO2. Images were acquired on either a Photometrics Coolsnap HQv2 CCD camera (Photometrics, Tucson, AZ) or Andor Zyla 4.2 CMOS camera (Andor Technology, Belfast, UK).

Image Segmentation: Images were segmented using custom Matlab code which can be provide upon request. The main algorithm performs initial segmentation using the Phase Stretch Transform algorithm developed by the Asghari and Jalali (Asghari and Jalali, 2015). Phase stretch images were thresholded and skeletonized to obtain cell outlines. Broken edges in the skeleton were repaired using a modified implementation of edgelink developed by Peter Kovesi ("Peter's Functions for Computer Vision," n.d.). After edge-linking the remaining unclosed portions of the path were removed. The interior of each cell is checked for high intensity features which typically indicate under-segmentation. Any region containing a high intensity region within the boundary are discarded. The above algorithm has 4 parameters describing the PST parameter set and the interior threshold. Parameters were first optimized by hand. We then randomly generated 1000 parameter sets around these values. We generated a rough ground truth segmentation by averaging over several parameter sets which we verified to segment the images well. The 1000 parameter sets were checked against this ground truth to choose a final parameter set. This parameter set was used to segment all images analyzed in this paper. Examples of the segmented outlines overlaid on the fluorescence images are found in the supplement (Movie S8).

Cell tracking: Cell tracking was performed using established particle tracking methods (Crocker and Grier, 1996). Cell centers were determined by taking the centroid of each region in the cell outlines generated as described above in Image Segmentation. The particle trajectories were compiled from these position

measurements using SimpleTracker, a Matlab function developed by Jean-Yves Tinevez ("Simple Tracker - File Exchange - MATLAB Central," n.d.). For each image in a given time series the average displacement was determined and was subtracted from the cell positions to account for stage drift between each frame. We determined a lower bound on the tracking error by tracking image series of fixed cells (Fig. S9)

For each movie the cell position, shape, magnitude of displacement at a 10-minute interval, and cell area were determined for each individual cell over all time points. The average magnitude of displacement was calculated for each field of view at each time point to obtain a cell speed. The inverse of the average area was calculated to determine cell density in each frame. We computed displacements squared at all subsequent images in the time series and averaged across the dataset to produce a mean squared displacement curve (supplemental figure 4d). Cell positions, velocities and shapes obtained from the tracking were used to compute all correlation functions described in the following sections.

Measurement of Cell Shape: We benchmarked a variety of algorithms for determining perimeter and area and found many give rise to large systematic errors. We have chosen to report the shape of a polygon reconstructed from identified cell vertex locations which we found to be the most accurate and robust metric (Fig S1, supplemental discussion). Shape parameter was computed for each cell based on the perimeter and area of a polygon constructed from cell vertex locations. The vertex locations parameterize the vertex model and therefore also allow for direct comparison with the model. Reconstructing a polygon from vertices also removes resolution dependent ambiguity in perimeter measurement (Coastline Paradox).

Vertex locations were found by locating branch points in the segmentation mask generated as described in Image Segmentation using the built in Matlab bwmorph function. Cells which do not have a complete set of segmented neighbors also do not have a complete set of vertices and therefore were discarded. We measured average cell shape for the full set of cells and cells remaining after discarding edge cells and found only a small difference in the average. We believe this difference comes from a small segmentation bias for cells whose outline is not correctly constrained by the neighbor. Therefore, the interior cell shapes are likely slightly more accurate. The shape parameter q = perimeter/sqrt(area) was measured by computing perimeter and area for the reconstructed polygon. The shape parameter is related to the another popular shape metric – circularity = 4*pi*area/perimeter^2 = 4*pi/q^2. Final cell shape was determined for each experiment by averaging the shape parameter for all fields of view measured to have a speed below 0.04µm/min. This final shape value is within a few percent of the value obtained by fitting the shape vs time curves to an exponential decay.

Simulation methods: We perform numerical simulations of monodisperse thermal Voronoi models, as described in (Sussman, 2017). Briefly, we begin by writing down a dimensionless form for the standard vertex model energy, $= \sum_{i=1}^{N}[k_A(a_i - a_0)^2 + (p_i - p_0)^2]$. This simple expression assigns an energy to the cells in a confluent monolayer in terms of their preferred geometry. The energy depends on the area a_i and perimeter p_i of each of the N cells (indexed by i), which are determined by a Voronoi tessellation of the cell positions. The unit of length in the simulations are defined such that the average cell area is unity, and we also set both the preferred area $a_0 = 1$ and the stiffness parameter $k_A = 1$. The preferred value for the cell perimeter, p_0, then constitutes the remaining control parameter which sets the target state of the monolayer.

We then use the cellGPU package to simulate overdamped Brownian dynamics of the model at different temperatures, T. The curves in figure 2 (Fig. 2c) were created by performing an ensemble average over approximately 30 independent systems of $N = 1000$ cells at each (p_0, T) point in parameter space along the lines indicated in (Fig. 2b). Each system was initialized in a high-temperature configuration and then allowed to equilibrate at the target temperature for a large multiple of the system's

characteristic relaxation time, as estimated from the data in Ref. (Sussman et al., 2018); after this equilibration period the observed average shape parameter of the cells and mean-squared displacement at several typical time lags was evaluated.

Preparation of Fibroblast conditioned Medium: Fibroblast conditioned medium was prepared as described previously. We cultured a 10 cm dish of MEF cells to confluence. Cells were washed and 20 mL of fresh medium was added to the cells. 48 hours later the media was collected and centrifuged to remove any cells. The MEF cells were then discarded. Conditioned media was aliquoted and frozen at -20C then used within 1 month of preparation. The conditioned medium was mixed 50:50 with fresh culture medium and added to MDCK cells 15 minutes after plating. We tested that fibroblast conditioned medium caused cell scattering of small colonies on collagen coated glass substrates as previously described (Stoker et al., 1987).

Cell division tracking: We found that our cell tracking consistently does not follow cell trajectories through a cell division because the distance threshold of trajectory linking is significantly larger than a cell radius. We exploit this to identify cell divisions and to measure shape change independent of cell division (Fig. 5d, Fig. S7). We identified cell divisions by identifying pairs of cells which appear in adjacent to each other in a frame after both cells were not present in the previous frame. We further filter out cells which are not of similar size to one another. We confirmed by inspection that this gives us a subset set of cells which have divided in the previous frame with few false positives. We then find the mother cell by looking several frames back for a cell near the centroid of the pair of daughter cells. We identify neighbors adjacent to both or one of the daughter cells and track each of these cells back in the trajectory to compare cell shapes before and after the division. We then average across all cell divisions in the dataset to produce the final values (figure 5e).

Calculation of mean squared displacements: Particle trajectories were compiled as described in the Particle Tracking section of the methods. We took each trajectory and decomposed it into non-overlapping sub trajectories starting from the initial time point with length ranging from tau = 10 minutes to the full trajectory length. The average displacement squared for each sub trajectory was computed and averaged across the dataset (Fig. S5d). To compute the time averaged mean squared displacement averaging was done for all sub-trajectories of a single particle and each cell with a full trajectory is plotted (Fig S2a). To plot mean squared displacement against time we averaged for a given value of tau and t across the dataset (Fig. S2b).

Three Pixel vector method of measuring perimeter and area: The three pixel vector method was implemented as previously described (Inoue and Kimura, 1987). Briefly, the different ways of linking pixels are divided into 4 classes and 13 subclasses. Each subclass has a defined length giving a 1x13 vector. For each class there is a linking correction depending on the difference of the direction of the current and subsequent vector which is specified by a 4(classes)x16(directions) matrix. To determine the areas enclosed by each vector we sketched the set of 13 available classes of linking and computed the area of edge pixels and pixels outside the polygon for each case. We obtained the values [2,3,2,2,2,2,3/2,1,11/4,3,2,3/2,2]. We then inferred area corrections for each class from their respective perimeter corrections linking as follows : [0,0,0,0,1/2-2,1-1/2,2-2,0,2,2,2,2,1,1,1,1]; [0,0,1/2-2,1/2-2,2-5,0,0,2,2,2,1,1,1,1,0,0]; [0,-1,-1,2-2,0,0,0,0,2,1,1,1,1,0,0,0]; [0,0,0,1/2-2,2-2*1/2,2-2,0,2,2,2,2,1,1,1,1,0]. We compute the perimeter as described by Inoue et al. and using the same rules and values specified above plus the area of the interior pixels calculate the area of the polygon.

Field of View analysis: The shape vs speed for different size fields of view were computed by segmenting each field of view into a set of sub fields. To simplify this process first the field of view was

truncated into a square to make sub division possible in such a way that the same set of cells are always measured. Then the field was subdivided into 1, 2x2, 3x3… 10x10 regions. We computed the average speed and shape in each sub-region, then binned the results of all regions according to average speed in the region. To characterize noise in the correlation we computed the average deviation of the derivative in a linear region of the curve for shape parameters ranging from 3.93 to 3.97.

Measurement of neighbor exchange rate

To measure a neighbor exchange rate, we detected 4 fold vertices and computed the ratio of 4 fold to 3 fold vertices per unit time. Such 4 fold vertices are not stable in the system and thus result in either a successful or attempted neighbor exchange. Our method does not detect the difference between successful neighbor exchanges and attempts which resolve in the original direction. A 4 cell vertex after formation was observed to resolve in either direction within at most 10 frames. Therefore, we iterated through each set of outlines and detected all 4 cell vertices. We discarded detections which happened within 10 pixels and 10 frames of a detected event to avoid double counting due to time delay between formation and resolution. This set of candidate events contained many false positives where the outline appeared to have a four-fold vertex but upon inspection of the raw data we observed a short 3 cell vertex. To remove these false positives, we manually sorted through the 4 cell vertex candidates and selected out real events.

Supplemental Discussion

Shape Metric Benchmarking - **Common Shape Metrics are resolution Dependent**

In the initial analysis we noticed an unexpected density dependence of cell shape which had a different magnitude depending on which metric we used for measuring shape. We therefore decided to benchmark methods of measuring object shapes in digital images. Measuring the shape of polygonal objects projected onto a pixel grid is nontrivial because segmented edges are limited to single pixels while the actual object edge is a subpixel feature. Data is recoded on a 6.45µm/pixel camera at 20x magnification giving 0.3225 µm/pixel final resolution for a cell radius of ~15µm. Therefore, the edge of a cell contains few enough pixels that choice of shape metric is important. The simplest method to determine a length in an image made of pixels is to count the number of pixels along the perimeter. A more sophisticated method count pixels at 0, 90,180,270 degree angles (even) as a distance 1 and diagonal (odd) pixel connections as sqrt(2). This method is used to determine perimeter in the popular image processing software imageJ. This method overestimates the length where even and odd edges meet. Another method developed by Vossepoel uses a correction factor for pixels which change from odd to even with parameter values fit from simulated images of lines. This is used in the built in perimeter determination in regionprops in Matlab. This correction factor is not always accurate for small polygons. The corner correction can also be made by estimating that these connection have length sqrt(5) although this method does not correctly capture the length of some corner corrections. The Three Pixel Vector method developed by Inoue and Kimura explicitly implements all possible corner corrections (Inoue and Kimura, 1987). Object areas also can be measured in several ways. The most common method is to add up all the pixels in the polygon which the default method used in ImageJ and Matlab. This method overestimates the area of the polygon as it encloses area outside of the corrected perimeter contours described above. Instead the area can be measured by constructing the contours described above and finding the enclosed area.

To measure shape we implemented several of the methods described above. We also implemented an additional method which is specific to our dataset, where the objects can be defined by simple polygons constrained by the cell vertices. To measure this polygon shape we measure vertex locations estimated to the nearest pixel and reconstruct the polygon by connecting the vertices by straight lines. The vertex locations were determined by locating branch points in the cell outlines. One drawback of this method is that segmented cells which do not have a complete set of neighbors lack a complete set of vertices and must be discarded. For every cell with a complete set of neighbors, the vertices belonging to each cell were determined. The perimeter and area of a polygon defined by a set of vertex locations can be computed directly without lines being interpolated on to a grid of pixels. A representative image of the vertex locations on the membrane GFP image are displayed (Fig. S1b).

We compared the relationship between cell shape and density which reveals the presence of resolution dependent artifacts at increased density (Fig S1c). We observe a larger density dependence for more simple methods of perimeter and area determination which are known to produce large resolution dependent errors. The methods from three pixel vector closely match the vertex reconstruction – we infer that these are the two most accurate methods. We confirmed these findings by generating simulation images from the thermal voronoi model with known shape parameter and measuring the cell shapes (Fig

18

S1d). This confirms that TPV and vertex reconstruction typically have less than 1% error. Finally, we segmented images of fixed cells (Fig S9) and measured the cell shape over a trajectory. This shape should be constant because there is no motion in the images only small changes in signal to noise and small stage drifts. We compared the measured values across each trajectory to the mean and observe larger fluctuations in the TPV method (Fig S1e). This indicates that small differences in the segmentation boundaries can lead to relatively large errors in the final value of shape parameter. Therefore, the vertex reconstruction appears to be more robust to small changes in the signal. Although the vertex reconstruction requires discarding cells with an incomplete set of neighbors, for our 335x445 µm field of view and signal to noise the number of measurements (100-400 cells) is still large enough to provide a reliable average.

Cell Motility decreases with time

We observed that dynamics in the MDCK monolayers evolve with time. To confirm that individual cells show similar motile behavior we plot the time averaged mean squared displacement (TAMSD) (supplemental figure 2a). We observe qualitatively similar behavior for all cells in the monolayer. At short time scales the motion is nearly ballistic, however at later lag times the TAMSD plateaus for each cell. This indicates that at longer time scales most cells are confined by the neighboring cells and as a result do not end up traveling more than a few microns – only a fraction of a cell diameter. We also look at the time evolution of this motion by plotting the mean squared displacement as a function of time (supplemental figure 2b). We observe that for different lag times the mean squared displacement decreases. This shows that at later time points even for short time scales the diffusion is slower.

Correlation between shape and speed is not dependent on field of view size or lag time

From our active vertex model, we expect that shape parameter is useful for describing dynamics in the system. In the model, passive and active forces are defined at the level of single cells and therefore we expect that behaviors are mainly dictated by a cell and its nearest neighbors. The relationship between shape and speed should not be dependent on how the system is measured, meaning that the size of the field of view or lag time is somewhat arbitrary. We first test the relationship between the correlation we observe and the field of view size. We subdivide the field of view into at 335µm square, 2x2 168µm squares, … 10x10 35µm squares (Fig. S4a). These squares contain the same data but if the properties of the system were not uniform, the smaller partitions may show different behaviors. If the forces are defined at the cellular scale, as we expect from the model, this partitioning should not change the relationship between shape and speed. We observe that across all partitions the same final relationship is recovered (Fig. S4b). However, we see that there is less noise in the correlation curve when partitioning into smaller regions. Because the correlation curve is not linear and the field of view is not uniform, as we average over a larger area the average shape does not capture local shape variation which results in regions much faster or slower than the average. We plot the fluctuations in the correlation curve with respect to the average to describe this effect (Fig S4c). As we reduce the size of the region we see the curve becomes more smooth until we reach a noise floor at ~100µm. We anticipate that if we had lower noise of cell displacements and a full segmentation these fluctuations would continue to decrease to the scale of a few interacting cells.

We also wanted to ensure that this correlation is not dependent on the lag time within a range of timescales. We plot the mean squared displacement as a function of the shape parameter at the beginning of each trajectory (Fig S4d). We see that for each lag time there is still a relationship between shape and speed. We plot the relationship between shape and speed for one field of view at different lag times and see similar behavior (Fig S4e). The relationship shifts down because the motion is diffusive so as lag time

is increased by a factor of two displacement increase by a factor of sqrt(2). We also see the same trend for the ensemble averaged correlations (Fig S4f).

Cytoskeletal rescue experiments do not restore relationship between shape and speed

Across inhibitors tested we examined the relationship of shape and speed. A subset of these conditions is plotted (Fig S5). In general, we see that the relative relationship between shape and speed for a given condition is similar however the absolute values are all shifted in the inhibitor cases. One potential concern in these experiments is that cytoskeletal polarization may be perturbed (Akhtar and Hotchin, 2001; Bryant et al., 2014; O'Brien et al., 2001; Playford et al., 2008; Yu et al., 2003). Changes in cytoskeletal organization may affect how well the system is described by vertex models which assume the monolayer mechanics are dominated by cortical actin at the cell-cell junctions. We wanted to examine if these defects are related to changes in cell polarity observed for many of these inhibitors. We attempted rescue experiments based on published rescues of RAC and FAK knockdown experiments. It has been observed that RAC promotes apical basal polarity through its role in assembling laminin into the basement membrane (O'Brien et al., 2001). We seeded cells on a collagen gel with 1mg/ml matrigel to see if the inclusion of exogenous laminin in the matrix via the matrigel would rescue the relationship between shape and speed (Fig S6b). We observe the same relationship between shape and speed in the presence of matrigel. We also attempted inhibiting both FAK and ROCK at the same time. ROCK inhibition rescues wound healing in FAK knockdown cells and restores apical basal polarity (Bryant et al., 2014; Chen et al., 2002). We observe similar behavior in conditions with both inhibitors (Fig. S6a)

Neighbor exchanges rates are low

We measured the rate of neighbor exchanges for one wild type and one inhibitor dataset (Fig. S10a). We were not able to reliable measure neighbor exchange rates with automated analysis so we only made this measurement for these two datasets. These neighbor exchange rates range from 1-10 per hour per 1000 cells which seems low compared to observations from some phases of development where neighbor exchanges are important for tissue flow (Blankenship et al., 2006). We observe that neighbor exchange rates are shape dependent and lower in the inhibitor treated conditions at all shape parameters. This suggests that the rate of neighbor exchange also depends on the cell division fraction, or active stress in the system. We relate these neighbor exchange rates to observed velocity and observe a correlation (Fig S10b).

A metric q_{track} can be related to different modes of shape change

We wanted to confirm that the relationship between final shape and cell divisions was not simply the consequence of oriented cell division. We exploit the fact that q_{track}, the difference in cell shape between subsequent time steps ($q_{track}(t) = <q(t+1)-q(t)>$), measures certain forms of cell shape change while ignoring others. For a given time step we directly observe, by tracking, a subset of the shape change which occurs. We denote the two types of cell shape change, division based (Q2) and deformation based (Q1 / q_{track}). The observed subset selectively ignores cell divisions, because division results in large enough displacements that the trajectory is broken in our tracking algorithm. q_{track} also ignore a subset of shape changes where the cell is not segmented in the initial or subsequent frame which are of either type (Fig S7a). Importantly, only type 1 shape changes are observed in q_{track}. Therefore, as long as there is not a difference between the behavior of cells which are not segmented we can obtain the average value of a Q1 shape change for a give frame. We can also determine the total shape change by measuring shape in each frame over all cells. We show that the ratio of these two, multiplied by a small correction factor (~1%), gives a relationship for the relative value of non-division based shape change (Fig S7b, S7c). If this value were on average 0 we could explain the correlation in figure 5a by oriented cell division. We

observe values much larger than zero for this metric demonstrating there is an additional mechanism driven by cell divisions. Our calculation ignores the addition of a neighbor to cells adjacent to the dividing cell. We confirm that the shape change by q_{track} is several times larger than the shape change which would result from the gain of an additional neighbor (Fig S7d). We observe that this metric is nearly 1 across all average shape parameters for three datasets with very different division rates (Fig. S7e). We show that for one condition q_{track} is similar to the total shape change except at early time points (Fig. S7f). We also observe that the direct shape change before and after cell division is shape dependent in this dataset consistent with the deviations in q_{track} we observe at high shape parameter (Fig. S7g). We then show that there is not a strong correlation between the total number of cell divisions and the total change in shape parameter (Fig. S7h).

q_{track} values are consistent with junction length changes as the main source of shape change

We measured shape change along cellular trajectories $\Delta q_{track}(t) = <q(t+1)-q(t)>$ which we show measures deformation based changes and ignores oriented division effects (Fig. S7b; S7c). We then compare this to the total shape change between time points $\Delta q_{total}(t) = q(t+1)-q(t)$ to measure the relative contribution of junction length changes and oriented division (Fig. S7e). We observe a slight discrepancy between these two metrics at early times in the experiment. At these time points cell aspect ratios may be large enough for oriented division to cause a net decrease in cell shape (Fig. S7d). However, we observe at later time points the q_{track} metric which ignores oriented division effects is sufficient to capture nearly all shape change in the monolayer. Across conditions with different division fraction junction length change consistently explains a majority of shape change in the monolayer (Fig. S7e). Therefore, the relationship in figure 5b implies that in monolayers with higher division fraction there is additional cell shape remodeling which occurs as a result of differences in cell mechanical properties or active stress caused by cell division.

21

Supplemental Movie Descriptions

Movie S1: Representative time series from a WT monolayer on a 2mg/ml collagen gel. Tracked displacements and cell shapes are plotted as colormaps on the outline generated from segmentation. Time step is 10 minutes.

Movie S2: Representative time series from a WT monolayer on a 2mg/ml collagen gel (left) and on a 4mg/ml crosslinked gel (right). Time step is 10 minutes.

Movie S3: Representative time series from a monolayer treated with 100 µM RAC inhibitor NSC23766 on a 2mg/ml collagen gel. Tracked displacements and cell shapes are plotted as colormaps on the outline generated from segmentation. Time step is 10 minutes.

Movie S4: Representative time series from a WT condition (left) and with 50:50 Fibroblast conditioned medium to normal culture medium (right). Time step is 10 minutes.

Movie S5: Representative time series showing wash in and wash out of the CDK1 inhibitor RO-3306. The inhibitor was added at 5µM at 5:00 and washed out of the imaging chamber at 10:00. Colormap of cell speed is plotted on the segmented cell outlines. Time step is 10 minutes.

Movie S6: Representative time series showing behavior after addition of microtubule destabilizing compound Nocodazole. Nocodazole was added at 300nM at 4:00. Time step is 10 minutes.

Movie S7: Representative time series showing behavior after addition of DNA crosslinker Mitomycin C. Mitomycin C was added at 20µg/ml at 7:30. Time step is 10 minutes.

Movie S8: Representative movie showing the segmentation of a time series. Segmented cells are represented in pink and overlaid on the GFP signal. Time steps is 10 minutes. Movie duration is 800 minutes.

22

Bibliography

Akhtar, N., Hotchin, N.A., 2001. RAC1 regulates adherens junctions through endocytosis of E-cadherin. Mol Biol Cell 12, 847–862. doi:10.1091/mbc.12.4.847

Asghari, M.H., Jalali, B., 2015. Edge detection in digital images using dispersive phase stretch transform. Int J Biomed Imaging 2015, 687819. doi:10.1155/2015/687819

Bissell, M.J., 1981. The differentiated state of normal and malignant cells or how to define a "normal" cell in culture. Int Rev Cytol 70, 27–100. doi:10.1016/S0074-7696(08)61130-4

Blankenship, J.T., Backovic, S.T., Sanny, J.S.P., Weitz, O., Zallen, J.A., 2006. Multicellular rosette formation links planar cell polarity to tissue morphogenesis. Dev Cell 11, 459–470. doi:10.1016/j.devcel.2006.09.007

Bryant, D.M., Roignot, J., Datta, A., Overeem, A.W., Kim, M., Yu, W., Peng, X., Eastburn, D.J., Ewald, A.J., Werb, Z., Mostov, K.E., 2014. A molecular switch for the orientation of epithelial cell polarization. Dev Cell 31, 171–187. doi:10.1016/j.devcel.2014.08.027

Chen, B.-H., Tzen, J.T.C., Bresnick, A.R., Chen, H.-C., 2002. Roles of Rho-associated kinase and myosin light chain kinase in morphological and migratory defects of focal adhesion kinase-null cells. J Biol Chem 277, 33857–33863. doi:10.1074/jbc.M204429200

Crocker, J.C., Grier, D.G., 1996. Methods of Digital Video Microscopy for Colloidal Studies. J Colloid Interface Sci 179, 298–310. doi:10.1006/jcis.1996.0217

Elsdale, T., Bard, J., 1972. Collagen substrata for studies on cell behavior. J Cell Biol 54, 626–637.

Inoue, K., Kimura, K., 1987. A method for calculating the perimeter of objects for automatic recognition of circular defects. NDT International 20, 225–230. doi:10.1016/0308-9126(87)90245-8

Lang, N.R., Skodzek, K., Hurst, S., Mainka, A., Steinwachs, J., Schneider, J., Aifantis, K.E., Fabry, B., 2015. Biphasic response of cell invasion to matrix stiffness in three-dimensional biopolymer networks. Acta Biomater 13, 61–67. doi:10.1016/j.actbio.2014.11.003

Ng, M.R., Besser, A., Danuser, G., Brugge, J.S., 2012. Substrate stiffness regulates cadherin-dependent collective migration through myosin-II contractility. J Cell Biol 199, 545–563. doi:10.1083/jcb.201207148

O'Brien, L.E., Jou, T.S., Pollack, A.L., Zhang, Q., Hansen, S.H., Yurchenco, P., Mostov, K.E., 2001. Rac1 orientates epithelial apical polarity through effects on basolateral laminin assembly. Nat Cell Biol 3, 831–838. doi:10.1038/ncb0901-831

Peter's Functions for Computer Vision [WWW Document], n.d. URL https://www.peterkovesi.com/matlabfns/ (accessed 1.27.19).

Playford, M.P., Vadali, K., Cai, X., Burridge, K., Schaller, M.D., 2008. Focal adhesion kinase regulates cell-cell contact formation in epithelial cells via modulation of Rho. Exp Cell Res 314, 3187–3197. doi:10.1016/j.yexcr.2008.08.010

Simons, K., Fuller, S.D., 1985. Cell surface polarity in epithelia. Annu Rev Cell Biol 1, 243–288. doi:10.1146/annurev.cb.01.110185.001331

23

Simple Tracker - File Exchange - MATLAB Central [WWW Document], n.d. URL https://www.mathworks.com/matlabcentral/fileexchange/34040-simple-tracker (accessed 10.2.17).

Stoker, M., Gherardi, E., Perryman, M., Gray, J., 1987. Scatter factor is a fibroblast-derived modulator of epithelial cell mobility. Nature 327, 239–242. doi:10.1038/327239a0

Sussman, D.M., 2017. cellGPU: Massively parallel simulations of dynamic vertex models. Comput Phys Commun 219, 400–406. doi:10.1016/j.cpc.2017.06.001

Sussman, D.M., Paoluzzi, M., Cristina Marchetti, M., Lisa Manning, M., 2018. Anomalous glassy dynamics in simple models of dense biological tissue. EPL 121, 36001. doi:10.1209/0295-5075/121/36001

Trepat, X., Wasserman, M.R., Angelini, T.E., Millet, E., Weitz, D.A., Butler, J.P., Fredberg, J.J., 2009. Physical forces during collective cell migration. Nat Phys 5, 426–430. doi:10.1038/nphys1269

Walpita, D., Hay, E., 2002. Studying actin-dependent processes in tissue culture. Nat Rev Mol Cell Biol 3, 137–141. doi:10.1038/nrm727

Yu, H.H., Dohn, M.R., Markham, N.O., Coffey, R.J., Reynolds, A.B., 2016. p120-catenin controls contractility along the vertical axis of epithelial lateral membranes. J Cell Sci 129, 80–94. doi:10.1242/jcs.177550

Yu, W., O'Brien, L.E., Wang, F., Bourne, H., Mostov, K.E., Zegers, M.M.P., 2003. Hepatocyte growth factor switches orientation of polarity and mode of movement during morphogenesis of multicellular epithelial structures. Mol Biol Cell 14, 748–763. doi:10.1091/mbc.E02-06-0350

Zhu, M., Lerum, M.Z., Chen, W., 2012. How to prepare reproducible, homogeneous, and hydrolytically stable aminosilane-derived layers on silica. Langmuir 28, 416–423. doi:10.1021/la203638g